

A multiresolution method for climate system modeling: application of spherical centroidal Voronoi tessellations

Todd Ringler · Lili Ju · Max Gunzburger

Received: 15 July 2008 / Accepted: 6 October 2008 / Published online: 14 November 2008
© Springer-Verlag 2008

Abstract During the next decade and beyond, climate system models will be challenged to resolve scales and processes that are far beyond their current scope. Each climate system component has its prototypical example of an unresolved process that may strongly influence the global climate system, ranging from eddy activity within ocean models, to ice streams within ice sheet models, to surface hydrological processes within land system models, to cloud processes within atmosphere models. These new demands will almost certainly result in the develop of multiresolution schemes that are able, at least regionally, to faithfully simulate these fine-scale processes. Spherical centroidal Voronoi tessellations (SCVTs) offer one potential path toward the development of a robust, multiresolution climate system model components. SCVTs allow for the generation of high-quality Voronoi diagrams and Delaunay triangulations

through the use of an intuitive, user-defined density function. In each of the examples provided, this method results in high-quality meshes where the quality measures are guaranteed to improve as the number of nodes is increased. Real-world examples are developed for the Greenland ice sheet and the North Atlantic ocean. Idealized examples are developed for ocean–ice shelf interaction and for regional atmospheric modeling. In addition to defining, developing, and exhibiting SCVTs, we pair this mesh generation technique with a previously developed finite-volume method. Our numerical example is based on the nonlinear, shallow-water equations spanning the entire surface of the sphere. This example is used to elucidate both the potential benefits of this multiresolution method and the challenges ahead.

Keywords Voronoi diagram · Delaunay triangulation · Climate modeling · Multiresolution

Responsible Editor: Eric Deleersnijder

LA-UR-08-05303.

T. Ringler (✉)
T-3 Fluid Dynamics Group, Theoretical Division,
Los Alamos National Laboratory, Los Alamos,
NM 87545, USA
e-mail: ringler@lanl.gov

L. Ju
Department of Mathematics, University of South Carolina,
1523 Greene Street, Columbia, SC 29208, USA
e-mail: ju@math.sc.edu

M. Gunzburger
School of Computational Science, 400 Dirac Science Library,
Florida State University, Tallahassee, FL 32306-4120, USA
e-mail: gunzburg@scs.fsu.edu

1 Introduction

Climate system models (CSMs) are an increasingly important tool for assessing anthropogenic climate change. CSMs, along with observations and theory, form the basis for the Intergovernmental Panel on Climate Change (IPCC) Working Group 1 Assessment Reports that detail the anticipated consequences of rising concentrations of atmospheric greenhouse gases (International Panel on Climate Change 2007). While CSMs have been highly successful in interpreting observations, confirming theory and providing gross estimates of climate sensitivity, the climate modeling

community will be challenged in the coming decade to extend the utility of CSMs well beyond their current scope.

At least two drivers are pushing CSMs into new and expanding roles. The first is the increasingly urgent need to resolve scales and processes that are far beyond the current scope of these models. There are likely to be unresolved processes and currently misrepresented processes that have significant influence on the global climate system. Every component of the Earth system has its own prototypical example, ranging from eddy activity within ocean models (Hallberg and Gnanadesikan 2006), to ice streams within ice sheet models (Joughin et al. 1999), to surface hydrological processes within land system models (Newman et al. 2006), to cloud processes with atmosphere models (Tomita et al. 2007). All of these processes are not faithfully included in IPCC-class CSMs primarily due to lack of resolution; the degrees of freedom required to comprehensively simulate these processes are computationally prohibitive given the current (and foreseeable) resources.

The second driver pushing the evolution of CSMs is the rapidly growing demand for high-fidelity assessments of regional climate change driven by increasing concentrations of atmospheric greenhouse gases. As appreciation for the possible consequences of anthropogenic climate change improves, we are confronted with the need to characterize the regional aspects of climate change in order to support adaption and mitigation strategies. As indicated by the last chapter of the IPCC WG1 Fourth Assessment Report (AR4), the push in this direction is already underway (International Panel on Climate Change 2007). To be successful in providing the relevant information regarding regional climate impacts, CSMs will require significant increases in resolution, at least regionally, along with the incorporation of new processes.

The magnitude of the problem that must be addressed by the climate modeling community in order to transition from coarse-grain global CSMs to robust multiresolution CSMs is portrayed in chapter 8 of AR4. Every one of the 23 models contributing to AR4 utilizes an ocean model based on structured quadrilateral grids using low-order (\sim second-order) numerics based on compact finite-difference/finite-volume stencils (See Table 8.2.1 in AR4). In addition, as a group, these 23 models showed a rapid migration in their atmospheric component from global spectral methods to finite-volume methods built on traditional latitude–longitude grids. Not a single model contributing to AR4 utilized unstructured grids or multiresolution methods. So, while the scientific and societal needs for multireso-

lution CSMs are strikingly clear, the path to that end is not at all obvious.

CSM components are presently testing various types of quasiuniform tessellations (also referred to as grids or meshes) to discretize the surface of the sphere. These quasiuniform tessellations are a significant improvement over their predecessor, latitude–longitude grids, by removing both the strong grid-pole singularities and the accompanying numerical filters required to regularize these singularities. Various types of meshes have been proposed as alternatives to the traditional latitude–longitude grid. For example, the cubed-sphere, which offers the same topological structure as the latitude–longitude grid without the strong pole singularities, has been successfully implemented in various efforts (McGregor 1996; Adcroft et al. 2004; Nair et al. 2005). Voronoi tessellations (also referred to as geodesic, icosahedral or hexagonal grids) have sometimes been chosen for their remarkable uniformity and isotropy (Ringler et al. 2000). Finally, closely related to these Voronoi tessellations are the Delaunay triangulations that have been successfully implemented in an idealized setting and are now being integrated into full CSMs (Bonaventura and Ringler 2005; Comblen et al. 2008). While all of these methods have successfully removed the grid pole singularities associated with latitude–longitude grids, it is not clear that any of these methods, as presently formulated, will be able to meet the challenges outlined above.

By their nature, quasiuniform tessellations imply a substantial increase in computational costs with an increase in horizontal resolution. A halving of the nominal grid spacing implies an increase in computational cost of approximately a factor of eight; a factor of four arises from doubling the degrees of freedom in each of the horizontal directions and a factor of two arises due to halving the time step. The computational burden associated with increasing resolution everywhere within the domain quickly exhausts available computational resources. For example, conducting eddy-resolving ocean simulations as a part of century-long coupled climate simulations is impracticable now and will likely continue to be so for at least the next decade or more. The current NCAR coupled CSM (Collins et al. 2006) uses an ocean component model with a 320×384 grid and a time step of approximately 1 h. The eddy-resolving version of this ocean model uses a $3,600 \times 2,400$ grid and a time step of approximately 6 min (Maltrud and McClean 2004). The two configurations differ by a factor of about 1,000 in terms of their computational burden. Similarly daunting computational burdens are found in ice sheet modeling, surface hydrology modeling, and atmospheric modeling.

The obvious implication here is that CSMs will not be able to fulfill their expanding roles by *solely* using quasiuniform tessellations. The corollary to this assertion is that multiresolution schemes will be required if CSMs are to meet the growing challenges over the next decade. In many ways, ocean models are ahead of the other climate system components in developing models amenable to multiresolution modeling (e.g. Stuhne and Peltier 2006; Giraldo and Warburton 2008). Yet, even within the limited context of ocean modeling, a large gap remains between the idealized dynamical-core simulations conducted to date and the goal of full-physics simulations of the real ocean. Clearly, a host of scientific complexities arise as we begin to contemplate the construction of a multiresolution IPCC-class CSM.

The recent work of St-Cyr et al. (2007) clearly indicates that a successful multiresolution scheme requires attention to the combination of method and mesh. The authors develop a multiresolution mesh by implementing an adaptive, hierarchical nesting technique in which quadrilateral elements are bisected to locally increase resolution. When this adaptive meshing technique was used in combination with a high-order spectral method, the resulting multiresolution scheme produced positive results. Alternatively, when the same technique was used in combination with a low-order, finite-volume technique, the results were equivocal at best; adding degrees of freedoms did not reduce numerical solution error. The implication is that robust, multiresolution climate system components will require close attention to both the quality of the variable-resolution meshes and to the numerical techniques we place “on top” of these meshes.

An alternative to hierarchical nesting is to produce a smoothly varying tessellation. By their design, smoothly varying tessellations provide strong control over the spatial patterns of truncation error. While this control may be superfluous when used in combination with high-order methods, it may prove to be critically important when used with the low-order, finite-volume methods that are ubiquitous in IPCC-class component models discussed above. The primary purpose of this paper is to develop a class of robust, variable-resolution meshes, called spherical centroidal Voronoi tessellations (SCVTs), that have the requisite characteristics necessary to meet the present and future challenges of climate system modeling.

SCVTs contain a host of qualities that should produce tangible benefits in the context of climate modeling. First, SCVTs are a superset of the quasiuniform Voronoi tessellations currently being used in the climate modeling community (e.g., Randall et al. 2002; Satoh et al. 2008). Thus, SCVTs are a logical extension

to meshes already being utilized. Second, as discussed in Section 2, even nonuniform SCVTs always produce smoother, more locally uniform meshes as the degrees of freedom are increased. The implication here is clear; SCVTs offer a robust means of producing multiresolution meshes that are guaranteed to increase in quality as computational resources grow. As discussed in Section 3, the technique to produce variable-resolution SCVTs is intuitive and straightforward to implement. Finally, each SCVT is associated with a Delaunay triangulation. The positive attributes associated with the SCVTs are also present in the associated Delaunay triangulation. While a tremendous amount of work is required to translate these positive attributes into robust climate simulations, we begin the task here by taking two steps. First, we develop example meshes for several types of climate system components to demonstrate the method’s ability to produce high-quality, variable-resolution meshes in a diversity of systems. Second, we will demonstrate the ability of these meshes to reduce solution errors, at least locally, in the context of the shallow-water system.

The two primary purposes of this paper are the following: (1) to introduce the climate modeling community to the basic principles of SCVT and (2) to highlight the broad applicability of SCVT to climate system modeling. Section 2 introduces and develops the mathematical foundation for SCVTs. Section 3 develops real-world SCVTs in the context of ice sheet and ocean modeling. Section 4 combines our SCVT technique for the generation of multiresolution meshes with a low-order, finite-volume technique to produce a prototype multiresolution scheme that is broadly applicable to climate system modeling. We look toward future developments of SCVT and draw some conclusions in Section 5.

2 Centroidal Voronoi tessellations

2.1 Definitions

Let Ω denote an open domain or a piecewise smooth hyper-surface in \mathbb{R}^d and $\|\cdot\|$ the corresponding standard Euclidean metric for \mathbb{R}^d . Given a set of distinct points $\{\mathbf{x}_i\}_{i=1}^n \subset \Omega$, we define

$$V_i = \{\mathbf{y} \in \Omega \mid \|\mathbf{x}_i - \mathbf{y}\| < \|\mathbf{x}_j - \mathbf{y}\| \text{ for } j = 1, \dots, n \text{ and } j \neq i\}$$

for $i = 1, \dots, n$. Clearly, $\{V_i\}_{i=1}^n$ forms a tessellation of Ω , i.e., the union of \bar{V}_i spans $\bar{\Omega}$ written as $\cup_{i=1}^n \bar{V}_i = \bar{\Omega}$.

We refer to $\{V_i\}_{i=1}^n$ as the *Voronoi tessellation* or *Voronoi diagram* (Okabe et al. 2000) of Ω associated with the point set $\{\mathbf{x}_i\}_{i=1}^n$. A point \mathbf{x}_i is called a *generator* and a subregion V_i is referred to as the *Voronoi region* corresponding to the generator \mathbf{x}_i . The duality (in a graph-theoretical sense) of a Voronoi tessellation of Ω is the well-known *Delaunay tessellation*, which always consists of triangles/tetrahedra. Algorithms for the construction of corresponding Voronoi diagrams and Delaunay triangulations have been well developed (Okabe et al. 2000; Renka 1999).

Given a density function $\rho(\mathbf{x})$ defined on Ω , for any region $V \subset \Omega$, we call \mathbf{x}^c the *constrained mass centroid* of V with respect to Ω if

$$\mathbf{x}^c = \arg \min_{\mathbf{x} \in V} \int_V \rho(\mathbf{y}) \|\mathbf{y} - \mathbf{x}\|^2 d\mathbf{y}. \quad (1)$$

The existence of solutions of Eq. 1 can be easily obtained using the continuity and compactness of the object function; however, solutions may not be unique. It is worth noting that, if Ω is an open domain or a flat hyper-surface, then \mathbf{x}^c coincides with \mathbf{x}^* , the *standard mass centroid* of V defined by

$$\mathbf{x}^* = \frac{\int_V \mathbf{y} \rho(\mathbf{y}) d\mathbf{y}}{\int_V \rho(\mathbf{y}) d\mathbf{y}}$$

that is much easier to compute.

A Voronoi tessellation of Ω is called a *constrained centroidal Voronoi tessellation* (CCVT) (Du et al. 2003a) if and only if the points $\{\mathbf{x}_i\}_{i=1}^n$ that serve as the generators of the associated Voronoi tessellation

$\{V_i\}_{i=1}^n$ are also the constrained mass centroids $\{\mathbf{x}^c\}_{i=1}^n$ of those regions, i.e., if and only if

$$\mathbf{x}_i = \mathbf{x}_i^c, \quad i = 1, \dots, n. \quad (2)$$

We often refer to the relation (2) as the *centroidal Voronoi tessellation* (CVT) property. The dual Delaunay grid is then called *constrained centroidal Voronoi Delaunay triangulation*. We remark that, when Ω is an open domain in \mathbb{R}^d , $\{\mathbf{x}_i, V_i\}_{i=1}^n$ is often just called a *CVT* (Du et al. 1999).

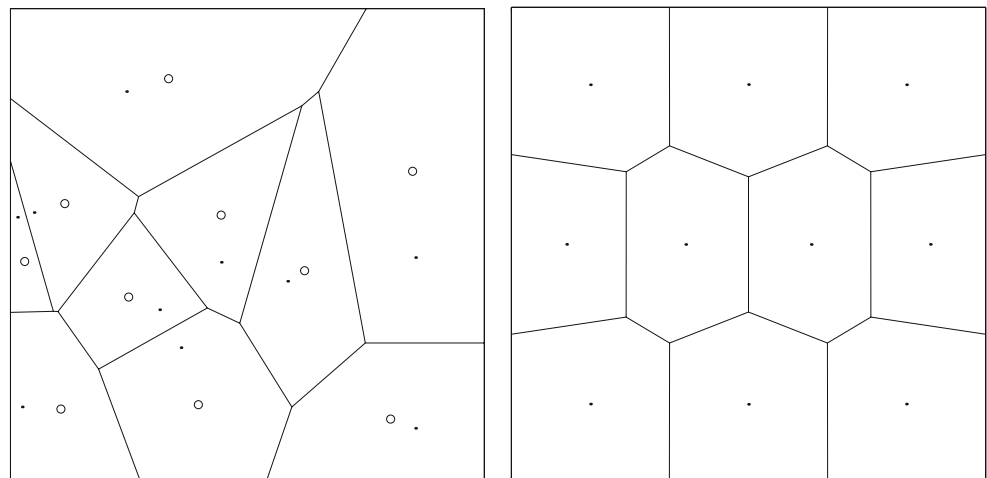
A very important case should be specially addressed for the application of CVT/CCVT to climate system modeling, that is, Ω denotes the surface of a sphere in \mathbb{R}^3 or part of it. In this case, we often refer to $\{\mathbf{x}_i, V_i\}_{i=1}^n$ as a *SCVT*. It is easy to verify that

$$\mathbf{x}^c = r \frac{\mathbf{x}^*}{\|\mathbf{x}^*\|}, \quad (3)$$

where r denotes the radius of the sphere, so that \mathbf{x}^c can be easily computed by first determining \mathbf{x}^* .

General Voronoi tessellations do not satisfy the CVT property; see Fig. 1 for an illustration. A square domain is randomly seeded with ten points (dots in Fig. 1, left panel). These ten points serve as generators for the Voronoi tessellation (cell boundaries in Fig. 1, left panel). For each Voronoi region, the standard mass centroid (open circles in Fig. 1, left panel) is computed. As discussed below in Section 2.3, a simple iterative calculation *regularizes* the initial Voronoi diagram on the left to the diagram shown to the right. In this example, we used a constant density to compute the standard mass centroid; a variable density field would have biased the resulting generator points toward the region of high density. This relationship between density and generator position is the key aspect of this grid-generation method.

Fig. 1 Left: a Voronoi tessellation of a square in \mathbb{R}^2 with 10 generators (the dots) randomly selected (the circles denote the centroid of Voronoi region); right: a 10-point CVT with a constant density function throughout the domain



2.2 Properties

Given any set of points $\{\tilde{\mathbf{x}}_i\}_{i=1}^n$ on Ω and any tessellation $\{\tilde{V}_i\}_{i=1}^n$ of Ω , we define the *energy* functional

$$\mathcal{K}(\{\tilde{\mathbf{x}}_i, \tilde{V}_i\}_{i=1}^n) = \sum_{i=1}^n \int_{\tilde{V}_i} \rho(\mathbf{y}) \|\mathbf{y} - \tilde{\mathbf{x}}_i\|^2 d\mathbf{y}.$$

The energy is often referred to as some physical quantity such as *variance*, *cost*, *distortion error*, or *mean square error* in practical applications. A priori, there is no assumed relation between the point set $\{\tilde{\mathbf{x}}_i\}_{i=1}^n$ and the tessellation $\{\tilde{V}_i\}_{i=1}^n$. However, it can be shown that $\mathcal{K}(\cdot)$ is minimized only if $\{\tilde{\mathbf{x}}_i, \tilde{V}_i\}_{i=1}^n$ is a CVT/CCVT (Du et al. 1999, 2003a). Thus, CVTs/CCVTs are Voronoi tessellations for which the generators are, in some sense, *optimally distributed*.

Let us set $\tilde{d} = d$ if Ω is an open domain and $\tilde{d} = d - 1$ if Ω is a hyper-surface in \mathbb{R}^d . Specially, for SCVTs, we have $\tilde{d} = 2$. As a consequence, CVT/CCVT meshes in \mathbb{R}^d have many good geometric properties, including the following (Du et al. 1999, 2003a; Du and Wang 2003):

- For a constant density function, the generators $\{\mathbf{x}_i\}_{i=1}^m$ are uniformly distributed across Ω .
 - Most Voronoi regions are (nearly) congruent (Gersho and Gray 1992; Du et al. 1999). Specially, for SCVTs, they are primarily convex spherical hexagons.
 - The mesh size h (as defined below in Eq. 5) is approximately proportional to $n^{-1/\tilde{d}}$
- For a nonconstant density function, the generators $\{\mathbf{x}_i\}_{i=1}^m$ are still locally uniformly distributed, and it is conjectured (and computationally verified) that, asymptotically,

$$\frac{h_{V_i}}{h_{V_j}} \approx \left(\frac{\rho(\mathbf{x}_j)}{\rho(\mathbf{x}_i)} \right)^{\frac{1}{\tilde{d}+2}}. \quad (4)$$

- The relationship between the relative sizes of Voronoi regions (i.e., grid cells) is controlled *entirely* by the specified density function.
- CVT/CCVT generators tend to accumulate in regions having relatively high values of ρ while remaining locally very regular.
- Thus, in principle, one could control the distribution of generators to minimize the error (either locally or globally) in the solution of a partial differential equation by, e.g., connecting the density function $\rho(\mathbf{x})$ to some a priori or a posteriori error estimates.

It is important to note that we are restricting our analysis and discussion to meshes generated with respect to an isotropic metric. We make this choice because we are currently interested in the methods ability to construct highly uniform, variable-resolution meshes. Extensions to anisotropic meshes have already been developed and are available for use in climate modeling if the need arises (Du and Wang 2005; Du et al. 2005).

2.3 Algorithms

Construction of CVT/CCVT is usually done by either probabilistic methods typified by MacQueen’s random algorithm (MacQueen 1967) (which is a simple iteration between sampling and averaging points) or deterministic methods typified by Lloyd iteration (Lloyd 1982) (which is a simple iteration between constructing Voronoi diagrams and mass centroids). Due to the low convergence rate of MacQueen’s method (MacQueen 1967), much attention has been focused on Lloyd method described below:

Algorithm 1 (Lloyd method) *Given a domain Ω , a density function $\rho(\mathbf{x})$ defined on Ω , and a positive integer n .*

0. *Select an initial set of n points $\{\mathbf{x}_i\}_{i=1}^n$ on Ω ;*
 1. *Construct the Voronoi regions $\{V_i\}_{i=1}^n$ of Ω associated with $\{\mathbf{x}_i\}_{i=1}^n$;*
 2. *Determine the (constrained) mass centroids of the Voronoi regions $\{V_i\}_{i=1}^n$; these centroids form the new set of points $\{\mathbf{x}_i\}_{i=1}^n$;*
 3. *If the new points meet some convergence criterion, return $\{(\mathbf{x}_i, V_i)\}_{i=1}^n$ and terminate; otherwise, go to step 1.*
-

Referring to Fig. 1, the process is as follows: The initial point set, shown as dots in the left panel, represents step 0. Step 1 is shown by the solid cell boundary lines in Fig. 1 (left panel). Step 2, the location of the cell centroids, is shown by the open circles in Fig. 1 (left panel) and forms the new point set from which we compute the new Voronoi diagram. The final result, after satisfying the convergence criterion in step 3, is shown in Fig. 1 (right panel). It should be noted that the mesh generation procedure utilizes, at most, the Voronoi diagram. While no reference to the Delaunay triangulation is required, the properties of smoothness and uniformity convey from the (S)CVT to the Delaunay triangulation.

2.4 Quality measure of Voronoi cells and Delaunay triangles

For the Voronoi cell V_i associated with the generator \mathbf{x}_i , we define its size to be

$$h_{V_i} = 2 \max_{\mathbf{y} \in V_i} \|\mathbf{x}_i - \mathbf{y}\|. \quad (5)$$

Then, h_{\max}/h_{\min} can be used to measure the global nonuniformity of the given Voronoi mesh where $h_{\max} = \max_i h_{V_i}$ and $h_{\min} = \min_i h_{V_i}$. In order to measure the local uniformity or quality of Voronoi cells of the SCVT, we use the following σ measure (Du et al. 2003b). For the Voronoi cell V_i associated with the generator \mathbf{x}_i ,

$$\sigma(V_i) = \frac{\min_j \|\mathbf{x}_i - \mathbf{x}_j\|}{\max_j \|\mathbf{x}_i - \mathbf{x}_j\|}, \quad (6)$$

where \mathbf{x}_j values denote Voronoi neighbors of \mathbf{x}_i . Clearly, $0 < \sigma \leq 1$ and $\sigma = 1$ correspond to the equilateral polygons. We then set

$$\sigma_{\min} = \min_i \sigma(V_i) \quad \text{and} \quad \sigma_{\text{avg}} = \frac{1}{n} \sum_i \sigma(V_i).$$

where n denotes the number of Voronoi cells. σ_{\min} measures the quality of the worst Voronoi cell and σ_{avg} measures the average quality of the Voronoi mesh.

In the Delaunay triangulation, the size of a triangle, T , is defined to be its longest side length, h_T . We apply the commonly used q -measure (Field 2000) to evaluate the quality of the dual triangular mesh (Delaunay triangles), where, for any triangle T , q is defined to be twice the ratio of the radius R_T of the largest inscribed circle and the radius r_T of the smallest circumscribed circle, i.e.,

$$q(T) = 2 \frac{R_T}{r_T} = \frac{(b+c-a)(c+a-b)(a+b-c)}{abc}, \quad (7)$$

where a, b , and c are side lengths of T . Clearly, $0 < q \leq 1$ and $q = 1$ correspond to the equilateral triangle. For a given triangulation, \mathcal{T} , composed of m triangles, we define

$$q_{\min} = \min_{T \in \mathcal{T}} q(T) \quad \text{and} \quad q_{\text{avg}} = \frac{1}{m} \sum_{T \in \mathcal{T}} q(T).$$

where q_{\min} measures the quality of the worst triangle and q_{avg} measures the average quality of the triangular mesh \mathcal{T} .

It is worth noting that the energy \mathcal{H} associated with the Voronoi tessellation $\{(\mathbf{x}_i, V_i)\}_{i=1}^n$ decreases monotonically during the Lloyd iteration if $\{(\mathbf{x}_i, V_i)\}_{i=1}^n$ has not reached a CVT/CCVT yet. In certain systems, or with certain methods, we may require nodes to be located on the boundary of the problem domain Ω .

CVTs/CCVTs and the above construction algorithm can be easily generalized so that some of the generators are constrained to lie on the boundary $\partial\Omega$ (Du and Wang 2003; Ju et al. 2006).

3 Example meshes

3.1 Land ice: Greenland

3.1.1 Motivation

The Greenland and Antarctic ice sheets are characterized by a wide range of spatial and temporal scales. In terms of spatial scales, each of these ice sheets spans several thousand kilometers. Interior regions of these ice sheets are characterized by relatively broad spatial scales on the order of 100 km or more. These interior regions are generally areas of net accumulation of mass due to atmospheric precipitation of water. As this net source of water is exported toward the ocean in the form of ice, relatively fast-moving ice streams form within each catchment zone. Not unlike their liquid water counterparts on land, these ice streams are long and thin with along-stream scales of several hundred kilometers and cross-stream scales often less than 10 km (Joughin et al. 1999). In addition, the shear zone separating the fast-moving ice streams from the adjacent nearly stationary ice is characterized by scales of 1 km or less. These ice streams transport the majority of ice volume from Greenland and Antarctica into the surrounding ocean (Rignot et al. 2008). As a result, robust predictions of sea-level rise will require an accurate simulation of ice stream dynamics. In fact, the recent IPCC WG1 AR4 document declined to draw substantive conclusions on the likelihood of rapid sea level rise during the twenty-first century because, in part, ice stream dynamics are not included in current ice sheet models (International Panel on Climate Change 2007).

In addition to the kinematically driven need for locally enhanced resolution, there is also a desire for increased resolution at the ice margin due to significant seasonal ablation. This is particularly relevant for Greenland, where intense melting occurs annually below 1,200 m. The subsequent transport of this meltwater to the bottom of the ice sheet may have a strong impact on basal sliding processes (Bell 2008). In the context of ice sheet modeling, we see both kinematics and physics as driving the need for locally enhanced resolution. Spatial resolutions below 1 km might be required for the accurate representation of these processes. When considering an entire ice sheet, a uniform

mesh of 1 km combined with the emerging three-dimensional Stokes solvers is not computationally tractable. So, instead, we turn to variable-resolution SCVTs to discretize this system.

3.1.2 Proxy for SCVT density

In this example, we will generate a mesh of Greenland that places enhanced resolution in the vicinity of ice streams. Our target resolutions for this grid are $h_{\min} = 2$ km in the vicinity of the ice margin and $h_{\max} = 100$ km in the interior; let $R = h_{\max}/h_{\min}$ represent the ratio of these target resolutions. Our estimates suggest that the resulting mesh will be computationally tractable for climate change simulations, even when used in combination with a full three-dimensional Stokes solver.

Figure 2 shows an observational estimate of surface ice velocity at a spatial resolution of 2.5 km (Bamber et al. 2000). The magnitude of velocity, $\|\mathbf{V}\|$, is presented on a \log_{10} scale and ranges from a minimum of approximately 0.1 km/year along ridgelines to over 10.0 km/year at the outlet of some ice streams. We use this observational data set in two ways. First, this data set allows us to define the location of the ice boundary of Greenland as a set of piece-wise linear loops (not shown) within which we develop the SCVT. Second, within each loop, we define the SCVT density function with the following sequence:

$$x = \log_{10}(\|\mathbf{V}\|), \quad x_{\min} = -0.5, \quad x_{\max} = 3.5 \quad (8)$$

$$x = \max(x, x_{\min}) \quad (9)$$

$$x = \min(x, x_{\max}) \quad (10)$$

$$\rho = \left(\frac{(x - x_{\min})}{(x_{\max} - x_{\min})} * R \right)^4 + 1 \quad (11)$$

We limit the lower bound on the SCVT density function such that all regions with surface velocities less than $x_{\min} = -0.5$ or 0.3 km/year receive the same resolution. We limit the upper bound on the SCVT density function such that all regions with surface velocities more than $x_{\max} = 3.5$ or 3 km/year receive the same resolution. Finally, density is normalized such that it ranges from 1 to R^4 to generate nominal grid cells spacings that vary by a factor of R ; see Eq. 4.

Figure 3 depicts the resulting Voronoi diagram using 25,936 nodes, resulting in a minimum resolution of approximately 4 km. Figure 4 shows the \log_{10} of the Voronoi cell area. We find broad regions of low resolution along the quiescent ice ridgelines with the vast majority of nodes placed in the vicinity of ice streams.

The color scale is saturated for all cell areas greater than 150 km² and for all cell areas less than 10 km². While 90% of the cells are spaced less than 10 km from their neighbors, 10% of the cells with grid spacing greater than 10 km cover approximately 40% of the ice domain.

We progressively add nodes into the domain until our target minimum grid resolution of 2 km is reached. Figure 5 shows the \log_{10} of Voronoi cell area using 101,115 nodes. In this figure, the color scale is saturated for all cell areas greater than 75 km² and for all cell areas less than 5 km². Figure 5 looks identical to Fig. 4; the only noticeable difference between the figures is the scale on the colorbar.

Table 1 presents the global quality metrics for the Greenland SCVTs. The quality histograms of the SCVTs are shown in Fig. 6. The bulk measures of uniformity shown in Table 1 show improvement in every category as resolution is increased. The histograms shown in Fig. 6 indicate a systematic shift toward higher mesh quality with increasing degrees of freedom. It is equally important that, as the number of nodes is increased, the histograms exhibit a noticeable reduction in the proportion of cells residing in the “low-quality” end of the histograms.

3.2 Ocean: North Atlantic

3.2.1 Motivation

Incorporating eddies into IPCC-class global ocean simulations remains a computational challenge. Eddy-resolving simulations typically require grid resolutions of approximately 10 km, implying approximately 5e6 degrees of freedom to span the global ocean surface. This is in stark contrast to typical IPCC simulations that currently use approximately 5e4 degrees of freedom to cover the same extent. The factor of 100 separating the two simulations is compounded by another factor of 10 since eddy-resolving simulations require a significantly shorter time step. The 1,000-fold increase in computational burden to move from resolutions presently used in IPCC-class simulations to global, eddy-resolving resolutions is currently beyond reach and will likely remain so for a decade or more.

An alternative and computationally tractable approach is to employ variable-resolution grids, such as SCVTs, to permit eddy-resolving resolutions at targeted locations. These variable-resolution grids could be employed in limited area domains or as part of a global ocean simulation. The ability to readily generate variable-resolution meshes for the global ocean system allows us to consider the notion of an optimal spatial

Fig. 2 Log base 10 distribution of ice velocity at the surface of the Greenland ice sheet (Bamber et al. 2000). The scale is saturated for all velocities above 10 km/year and for all velocities below 0.1 km/year

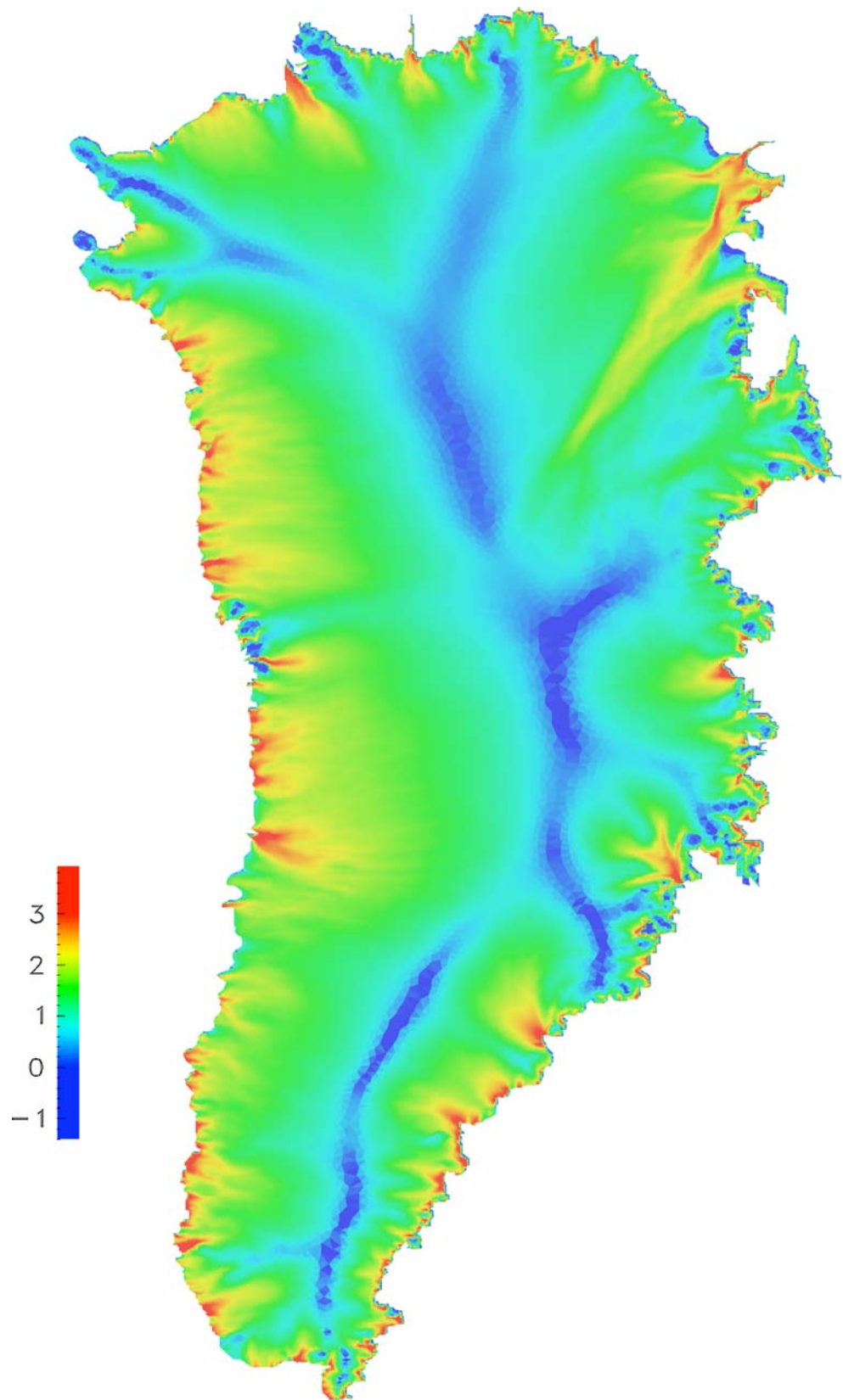


Fig. 3 A SCVT of the Greenland ice sheet using 25,936 nodes based on the density function given in Eq. 11. Note that grid cells within the ice streams are often too small to be visible

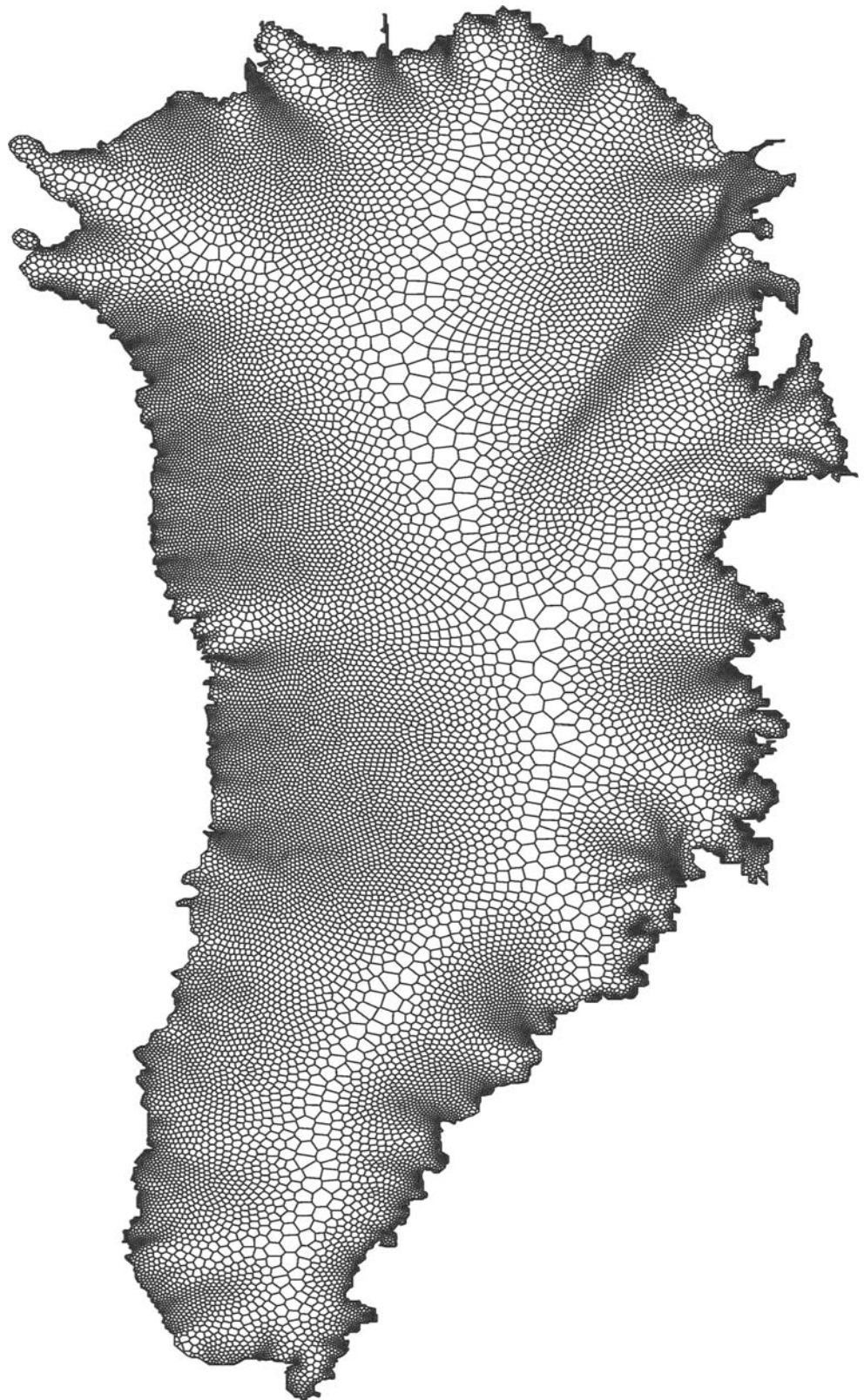


Fig. 4 Log base 10 distribution of Voronoi cell area of the Greenland ice sheet using 25,936 nodes. The scale is saturated for all cell areas above 250 km and for all cell area below 10 km

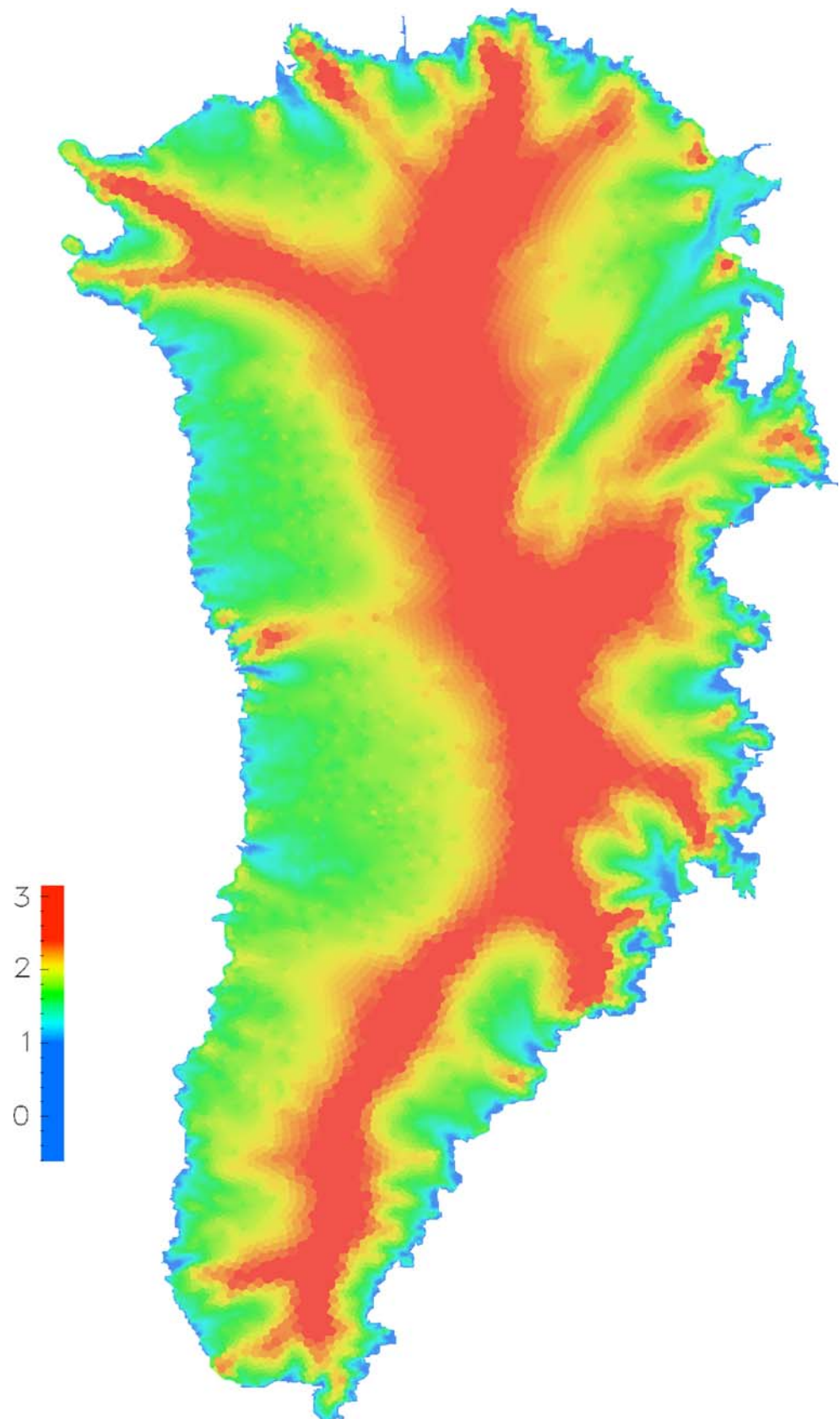


Fig. 5 Log base 10 distribution of Voronoi cell area of the Greenland ice sheet using 101,115 nodes. The scale is saturated for all cell areas above 65 km and for all cell area below 2.5 km

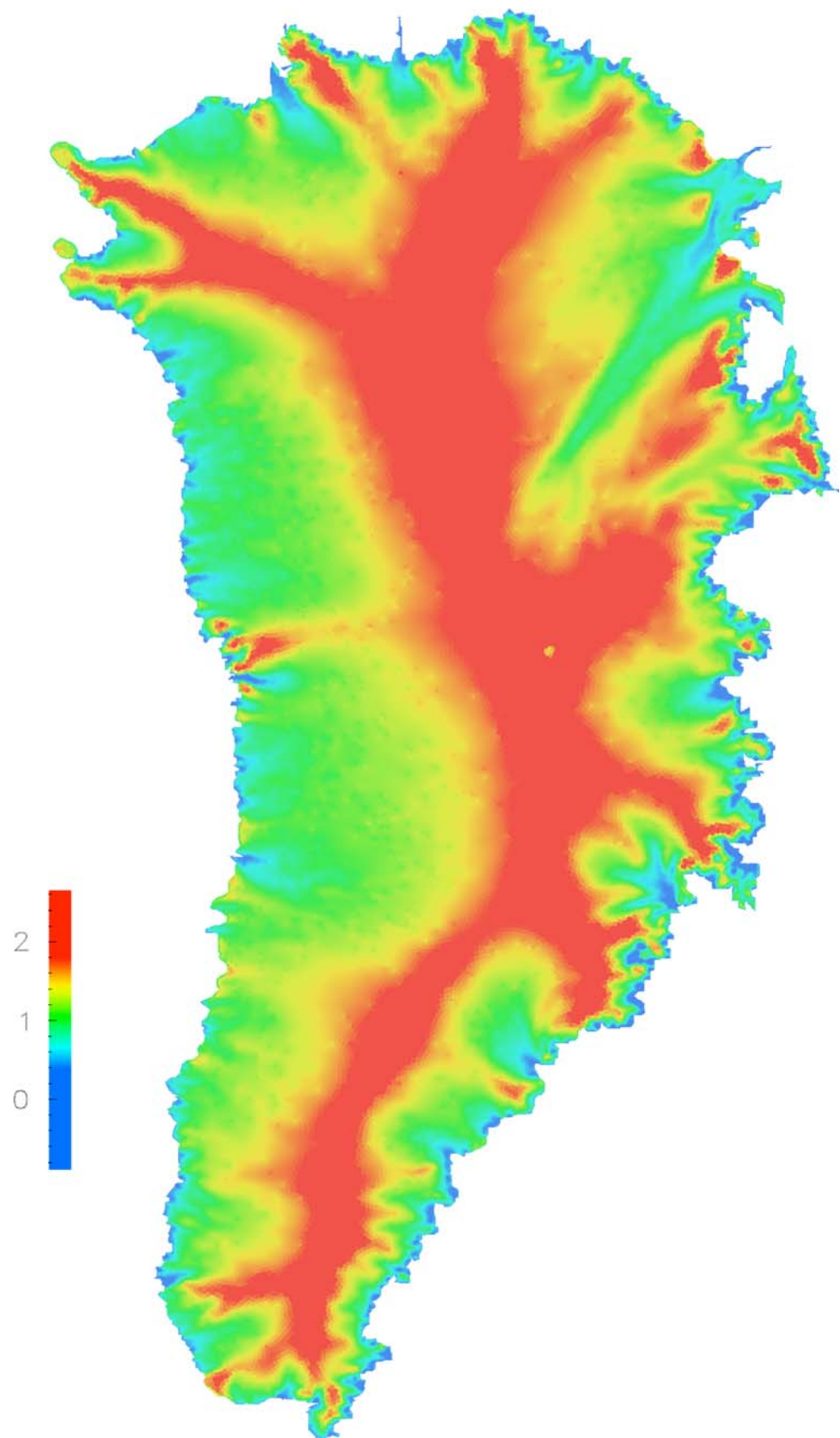


Table 1 Mesh information of SCVTs for the Greenland

Number of generators	σ_{\min}	σ_{avg}	h_{\max}/h_{\min}	Number of triangles	q_{\min}	q_{avg}
25,936	0.094	0.706	40.94	49,244	0.219	0.935
101,115	0.091	0.751	47.81	197,346	0.235	0.948

allocation of computation resources. In addition, the scientific study of many processes would surely benefit from the ability to support eddy activity in certain regions while maintaining a global ocean domain. Two supporting examples include the role of eddies on the meridional overturning circulation (Gnanadesikan 1999) and the role of eddies in mediating the ocean's response to changes in wind stress forcing (Hallberg and Gnanadesikan 2006).

3.2.2 Proxy for SCVT density

In this example, we will derive a variable-resolution mesh of the North Atlantic Ocean with sufficient resolution to resolve eddies within the major current systems. The domain is identical to the nominal 1/10 degree eddy-resolving simulation discussed in Smith et al. (2000). Using data from these simulations, we compute the time-mean kinetic energy of the surface

currents, as shown in Fig. 7. As can be seen in Fig. 7, the regions of intense eddy activity are extremely localized. Based on the kinetic energy, KE, we defined the density function as

$$x = \text{KE}/\text{KE}_{\max}, \quad x_{\min} = 0.1, \quad x_{\max} = 1.0 \quad (12)$$

$$x = \max(x, x_{\min}) \quad (13)$$

$$\rho = x^4 \quad (14)$$

where KE_{\max} is the maximum kinetic energy in the domain. The lower bound of 0.1 insures that a minimum resolution is maintained in the quiescent regions. The ratio $x_{\max}/x_{\min} = 10$ leads to a grid spacing that varies by approximately a factor of 10. In addition, we enhance the density function near the land–sea interface to insure that the boundary is adequately resolved. While we want the mesh to capture these regions of high activity via enhanced resolution, we also recognize the need to expand this region to allow eddies to travel

Fig. 6 Quality histograms of SCVTs of the Greenland ice sheet with 25,936 nodes (*top*) and 101,115 nodes (*bottom*). *Left*: Distribution of quality measurement of Voronoi cells σ ; *right*: distribution of quality measurement of Delaunay triangles q . Note the uniform shift toward higher-quality as the number of nodes is increased

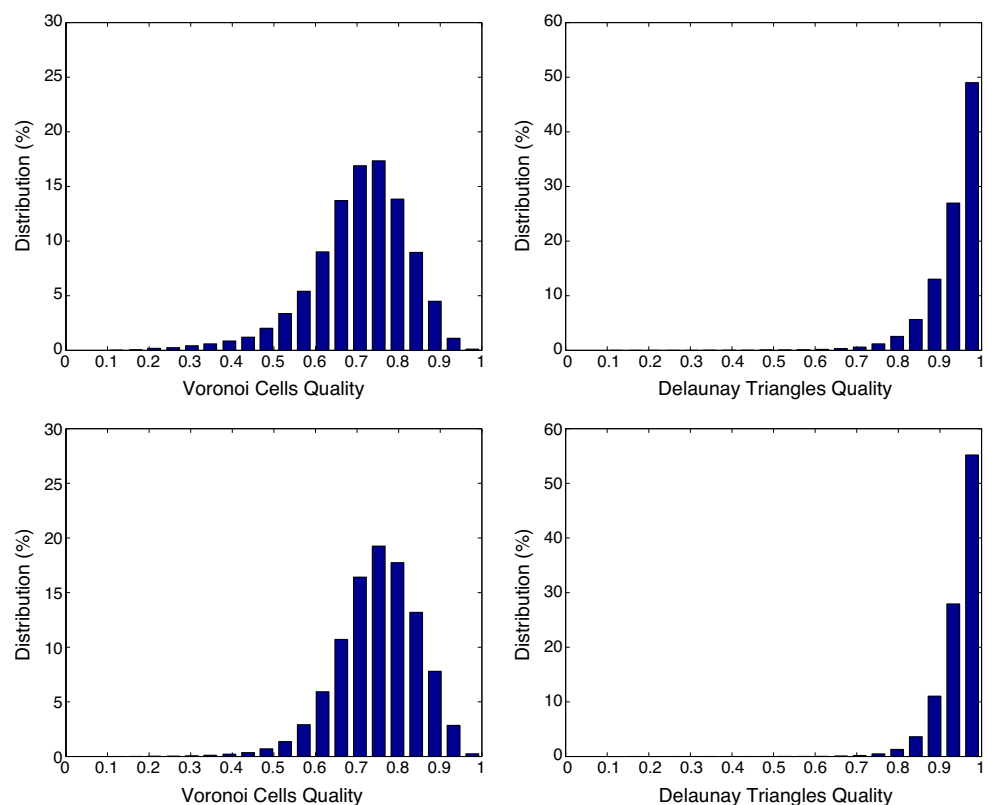
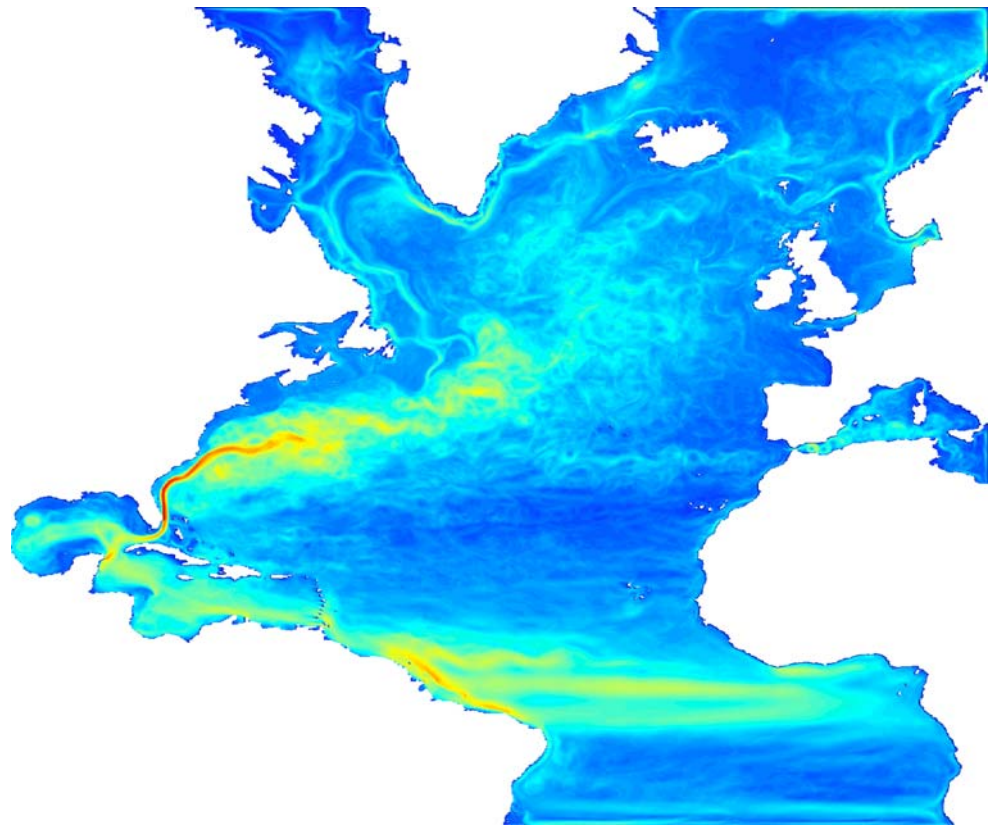


Fig. 7 Time mean kinetic energy from a global 0.1 degree simulation of the North Atlantic Ocean (Smith et al. 2000)



uninhibited by grid resolution. As such, we applied a substantial amount of Laplacian smoothing to our density function (approximately 20 passes) to expand and smooth the regions of enhanced resolution. (Note that the RMS of sea-surface height is also an accurate reflection of mesoscale ocean variability and we have developed global ocean SCVTs based on TOPEX remote sensing of sea-surface height.)

As with the Greenland example, we produced a continuous, piece-wise linear representation of the land–ocean boundary based on the land–sea mask used in the 0.1 degree simulation. This approach also identifies all islands. Islands with a circumference less than 10 km were discarded; the resulting domain contains 58 islands.

The Voronoi diagram shown in Fig. 8 uses 47,305 nodes. This results in a minimum grid resolution of approximately 20 km. We continue to add nodes into the domain until we reach a minimum resolution of 10 km. Closeups of this high-resolution mesh using 183,807 nodes and its low-resolution counterpart are shown in Fig. 9.

Table 2 presents the results of our North Atlantic SCVTs. The corresponding quality histograms are shown in Fig. 10. As with the Greenland example, the

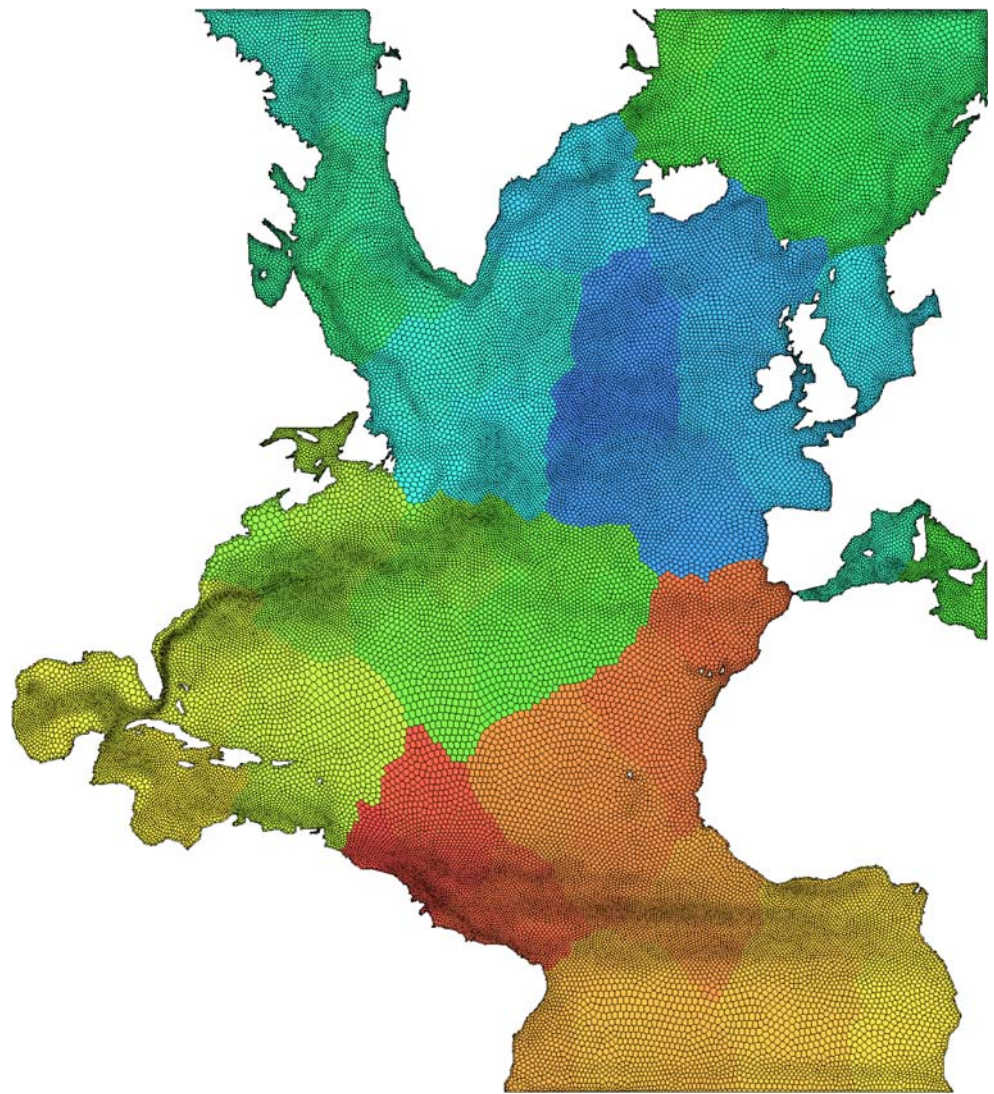
quality measures show a systematic improvement as we increase the degrees of freedom.

3.3 Ocean–ice shelf interaction

3.3.1 Motivation

Our final example couples ocean and ice domains in the context of ocean–ice shelf interaction. Ice shelves are ice flows that become ungrounded and buoyant and rest on top of ocean water. The location at which ice transitions from resting on bedrock to resting on ocean water is referred to as the grounding line. As the ice shelves are pushed outward into the ocean, the ice is either melted along the ice–ocean interface or calves from the main shelf into icebergs. These ice shelves provide a significant buttressing force that resists the flow of upstream, grounded ice. As evidenced by the Larsen B ice-shelf collapse, when the ice-shelf buttressing force is removed, the upstream ice flow can increase by several hundred percent (Rignot et al. 2004). The accurate simulation of ocean–ice shelf interaction is necessary in order to quantify the risk of rapid sea level rise (International Panel on Climate Change 2007).

Fig. 8 SCVT of North Atlantic ocean domain using 47,305 nodes. *Coloring* indicates the mesh decomposition for implementation on distributed memory systems: each *color* represents a separate computational unit



The West Antarctic Ice Sheet (WAIS) is particularly relevant to the study of ocean–ice shelf interaction. Not only are ice shelves the primary outlet of grounded ice, but the grounded ice frequently rests on bedrock that is increasingly below sea level as one moves toward the ice interior region (Schoof 2007). The physical geometry is such that a rapid erosion of the WAIS due to ocean–ice shelf interaction is a plausible scenario for the twenty-first century.

Ice shelves connected to WAIS have spatial extents of more than 1,000 km (e.g., the Ross Ice Shelf) down to less than 50 km (e.g., the Thwaites Ice Shelf). The embayments where this ice flows into the ocean have similar ranges in spatial scale. While the ice shelves are not as dynamically active as the ice streams that feed them, the structure and shape of the ice–ocean interface is a primary factor that drives mixing at this interface (Holland et al. 2008). Grid resolutions of less than 5 km are often used when simulating ocean–ice shelf

coupled dynamics. Furthermore, analysis of the global 1/10 degree ocean simulations in the vicinity of WAIS indicates that the transport of heat into these embayments may be eddy-driven and episodic (Maltrud, personal communication, 2007). Thus, resolving ocean eddies in and around these embayments will likely be required for robust simulations.

The horizontal discretization of this system is difficult because part of the domain will be ice (ice domain), part will be ocean (ocean domain), and part will be both ocean and ice (shelf domain). Furthermore, the characterization of a region as ice, ocean, or shelf will evolve over the time scales of decades to millennia. Due to this complexity and the fact that only limited work has been completed on modeling the coupled ocean–ice shelf system, we will explore techniques to discretize this system in an idealized setting. Figure 11 shows our idealized domain with a spatial extent of 1,100 by 550 km. The domain is characterized by a

Fig. 9 Close-up of Gulf Stream region using 47,305 nodes (*top*) and 183,907 nodes (*bottom*)

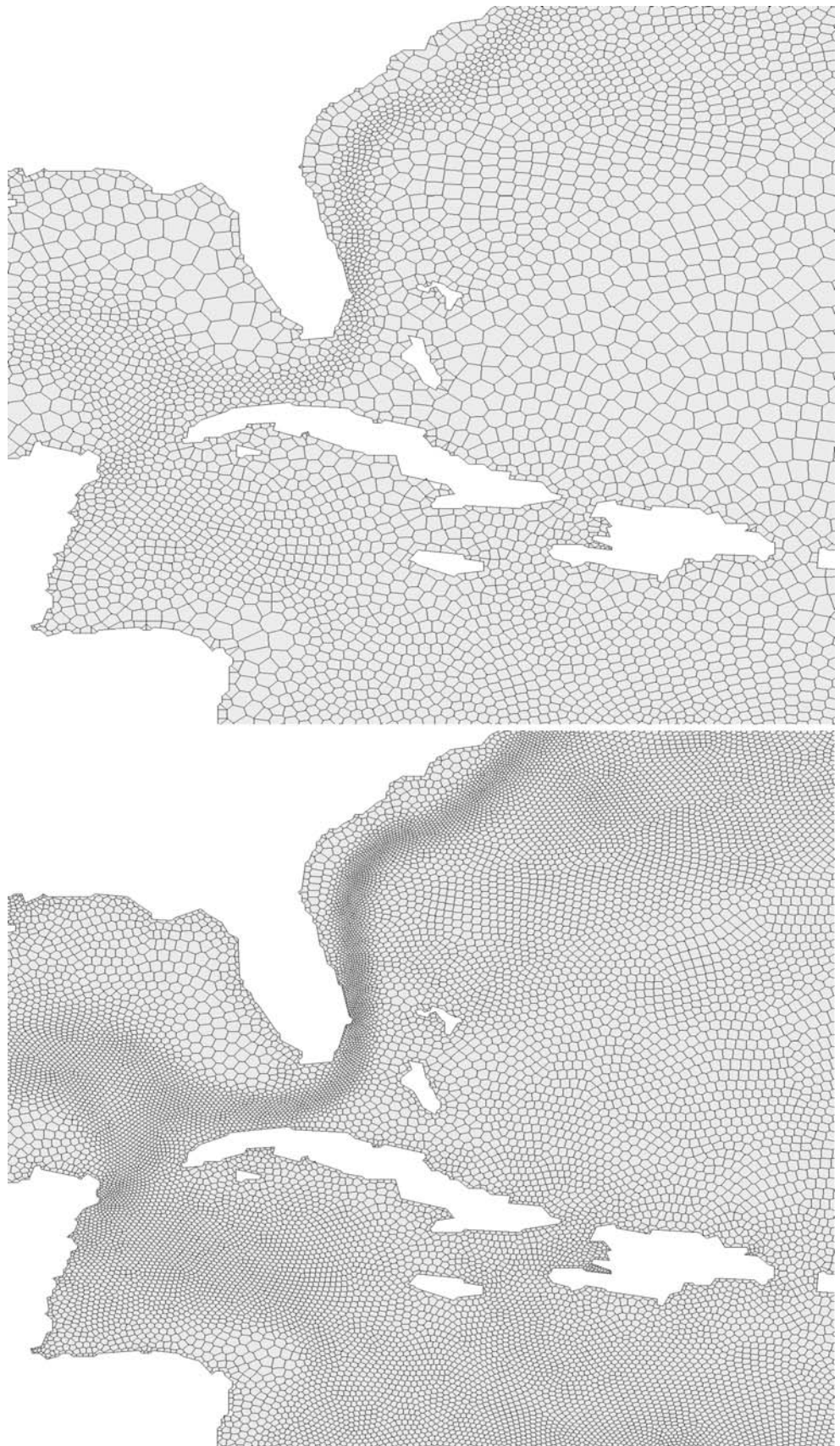


Table 2 Mesh information of SCVTs for the North Atlantic

Number of generators	σ_{\min}	σ_{avg}	h_{\max}/h_{\min}	Number of triangles	q_{\min}	q_{avg}
47,305	0.089	0.712	16.60	89,272	0.104	0.933
183,907	0.105	0.754	15.05	358,577	0.127	0.947

region of grounded ice (to the left), a region of ocean (to the right), and an ice-shelf region (center). The ice domain includes an ice stream that feeds the shelf region. As indicated in the figure, a robust simulation of this system will require enhanced resolution in the vicinity of the ice shelf, ice stream, and region of the ocean in proximity to the ice.

3.3.2 Proxy for SCVT density

In this idealized example, our intent is to produce a tessellation with a minimum grid spacing of 2 km and a maximum grid spacing of 20 km. As opposed to our other examples, we are not building our density function from a physical characteristic of the system. The generated density function has local maxima in the vicinity of the ice stream, in the region of the ice shelf, and along the entire ocean–ice boundary. The resulting Voronoi diagram of this system using 9,359 nodes is shown in Fig. 12 with a close-up of the shelf region at both high and low resolution shown in Fig. 13.

Table 3 presents the results on our SCVTs for the idealized ocean–ice sheet, and corresponding quality histograms are shown in Fig. 14. Yet again, the quality measure show increasing mesh quality with increasing degrees of freedom.

4 Example numerical method

The large majority of numerical methods utilized in IPCC-class climate models were developed in the context of uniform meshes. Successfully implementing these same numerical methods on nonuniform meshes, such as those developed above, will likely prove to be a difficult task, as discussed in St-Cyr et al. (2007). While emerging numerical methods based on spectral elements, discontinuous Galerkin, finite-element, or similar approaches are a more natural choice when considering the multiresolution meshes developed here, these alternative approaches are still relatively new to climate system modeling in comparison to low-order finite-volume methods. The sole purpose of this

Fig. 10 Quality histograms of SCVTs of the North Atlantic with 47,305 nodes (*top*) and 183,907 nodes (*bottom*). *Left*: Distribution of quality measurement of Voronoi cells σ ; *right*: distribution of quality measurement of Delaunay triangles q

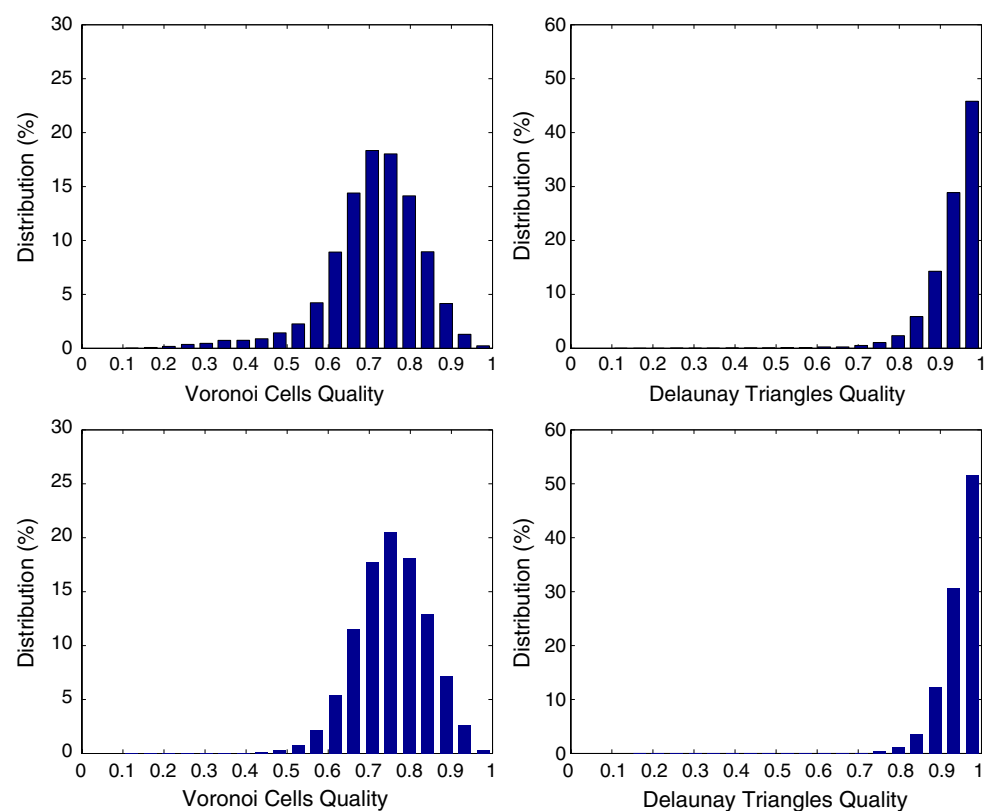


Fig. 11 An idealized ocean–ice shelf system. The ice domain (*left*) flows into the shelf region (*semicircle*) via an ice stream. Enhanced resolution in the vicinity of the ice stream, ice shelf, and ice margin will be required

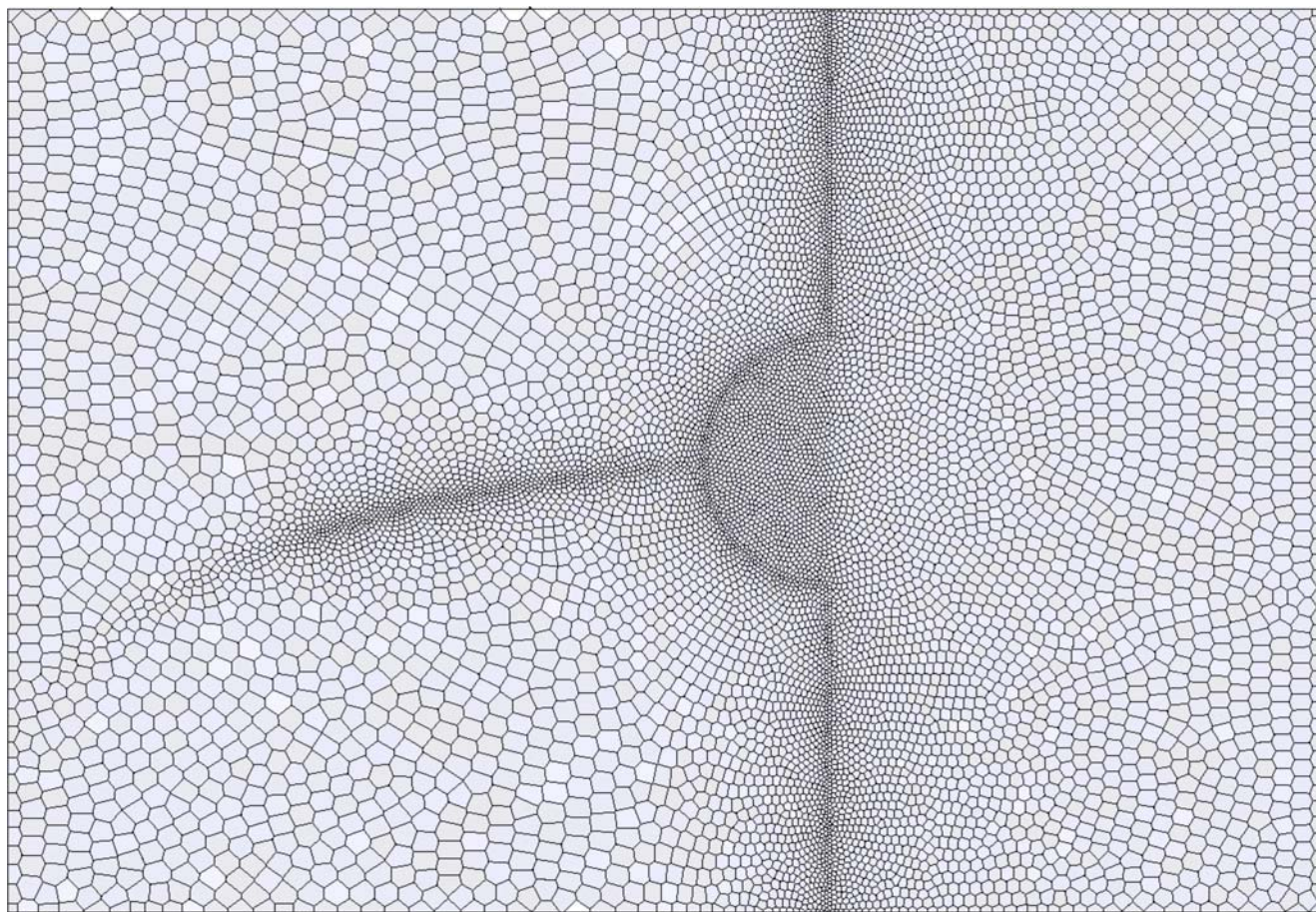
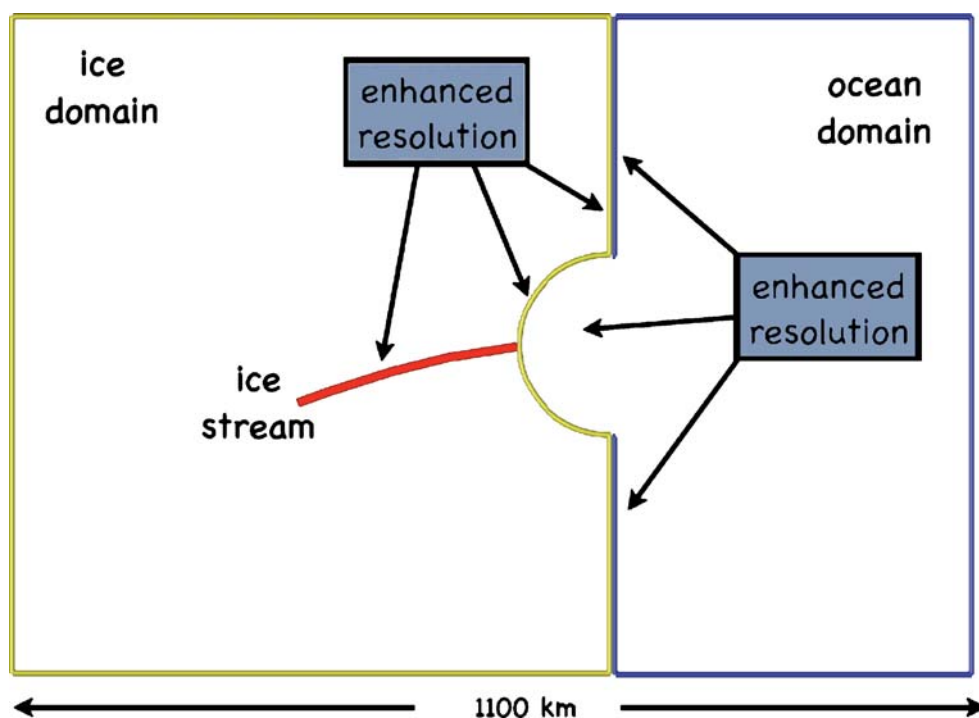


Fig. 12 SCVT of ocean–ice shelf system using 9,359 nodes. Note enhanced resolution in the vicinity of the ice stream, ice shelf, and ocean–ice interface

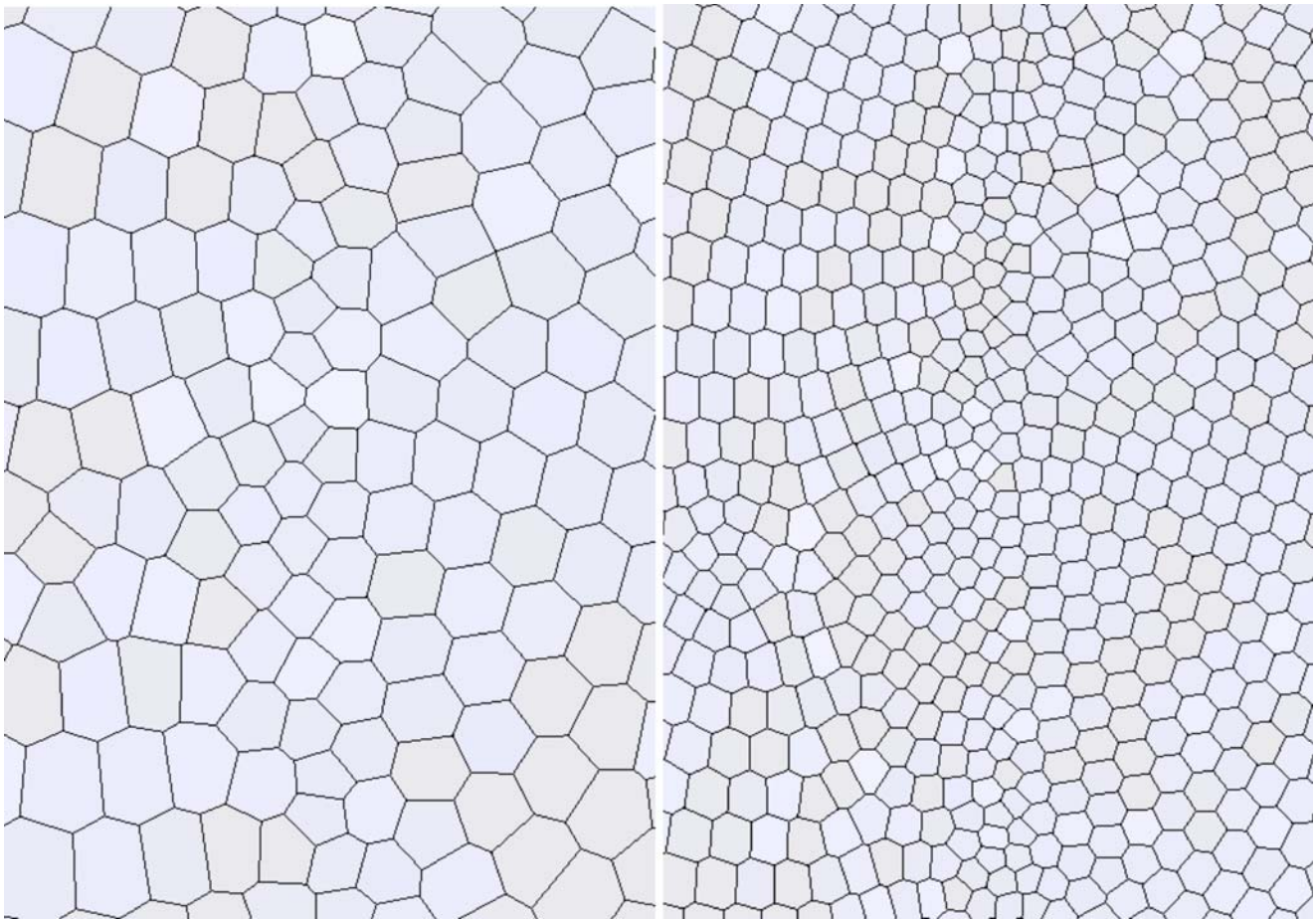


Fig. 13 Close-up of ocean-ice shelf SCVT in the vicinity where the ice stream enters the shelf region. *Left:* SCVT using 9,359 nodes. *Right:* SCVT using 37,157 nodes

section is to exhibit a low-order, finite-volume method capable of producing robust simulations when implemented on nonuniform SCVTs. The implication is that these meshes are immediately applicable to current-generation CSM components. With this purpose in mind, the discussion below is not intended to be exhaustive. In many respects, developing numerical methods that effectively utilize these nonuniform SCVTs is a much richer and more difficult problem than generating the mesh itself. While some efforts to exploit the local uniformity of SCVTs have already been completed (e.g., see Du and Ju 2005), much work remains. We have made significant progress regarding the formulation of finite-volume schemes suitable for implementation in these variable resolution meshes. These results will be detailed at a later time.

4.1 Continuous equations

For this demonstration, we choose the nonlinear, shallow-water equations spanning the entire surface of the sphere:

$$\frac{\partial h}{\partial t} + \nabla \cdot (h\mathbf{u}) = 0 \quad (15)$$

$$\frac{\partial \mathbf{u}}{\partial t} + (\omega + f)\mathbf{k} \times \mathbf{u} = -g\nabla(h + h_s) - \frac{1}{2}\nabla\|\mathbf{u}\|^2 \quad (16)$$

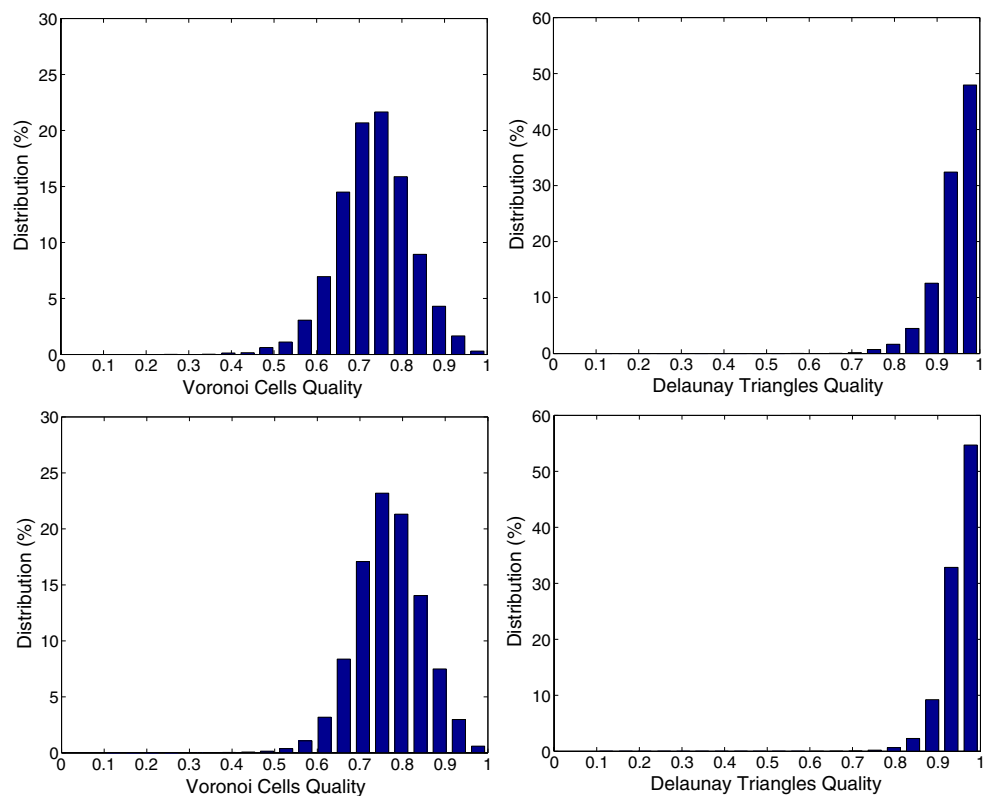
$$\omega = \mathbf{k} \cdot (\nabla \times \mathbf{u}) \quad (17)$$

where h is the fluid thickness, h_s is the height of the lower boundary, \mathbf{u} is the vector velocity orthogonal

Table 3 Mesh information of SCVTs for ocean-ice shelf system

Number of generators	σ_{\min}	σ_{avg}	h_{\max}/h_{\min}	Number of triangles	q_{\min}	q_{avg}
9,359	0.275	0.735	8.91	18,440	0.568	0.942
37,157	0.313	0.769	10.15	73,765	0.626	0.951

Fig. 14 Quality histograms of SCVTs of the idealized ocean–ice sheet with 9,359 nodes (*top*) and 37,157 nodes (*bottom*). *Left*: distribution of quality measurement of Voronoi cells σ ; *right*: distribution of quality measurement of Delaunay triangles q



to the local normal vector \hat{k} , and f is the Coriolis parameter. The component of relative vorticity in the plane normal to the surface of the sphere, ω , is defined in Eq. 17.

4.2 Discrete equations

We utilize the discrete method developed by Bonaventura and Ringler (2005). While the method developed in Bonaventura and Ringler (2005) is intended for use on multiresolution meshes, to our knowledge, this is the first demonstration. This method uses the Delaunay triangulation as the finite-volume cell for the thickness equation. The vorticity field is defined on the Voronoi diagram. Velocity components normal to the triangle edges are retained as prognostic equations. A schematic of this discretization is shown in Fig. 15. All quantities with overhats are derived fields, with \hat{T} representing the reconstructed tangent velocity required for the Coriolis force and $\hat{\eta}$ representing the absolute vorticity (see Bonaventura and Ringler 2005 for a full discussion). The discrete system is expressed as:

$$\frac{\partial h_i}{\partial t} = \frac{-1}{A_i} \sum_{j=1}^{\text{nedges}} \hat{h}_j N_j dl_j \quad (18)$$

$$\frac{\partial N_j}{\partial t} = \hat{\eta}_j \hat{T}_j - \left\{ \left[gh + gh_s + \hat{K} \right]_{i\text{Forward}} - \left[gh + gh_s + \hat{K} \right]_{i\text{Backward}} \right\} / dc_j, \quad (19)$$

where the summation in Eq. 18 is over the edges of each triangle. In terms of solution error, the scheme is nominally second-order accurate in space using centered-in-space reconstructions and fourth-order accurate in time using fourth-order Runge–Kutta time-stepping (see, e.g., Bonaventura and Ringler 2005). The simulations utilize no limiters, filters, or explicit dissipation of any sort. The center-in-space numerics, along with the fourth order Runge–Kutta scheme, is used to minimize any implicit diffusion.

We demonstrate this method on the two SCVTs shown in Fig. 16. Each mesh contains 40,962 nodes. The solid black line indicates the boundary of an orographic feature that is the sole forcing of the simulation (see below). The first mesh (top) is generated with a uniform density function leading to an average grid spacing of 120 km. The second mesh (bottom) is generated with higher densities in the vicinity of the orographic feature. The density function is chosen such that the average grid spacing is three times smaller (40 km) in the vicinity of the mountain than compared to its quasiuniform counterpart. The solid colors indicate our

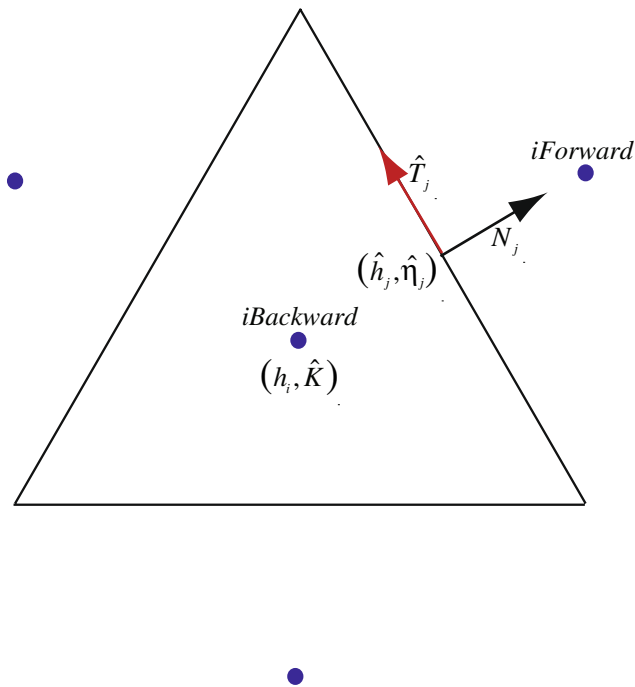


Fig. 15 A schematic of the finite-volume system. Thickness, h , and kinetic energy, \hat{K} , are defined at the center of the triangle. The normal component of velocity, N_j is defined at each cell edge. Vorticity, η , is defined at the triangle vertices. All quantities with overhats are derived fields, see Bonaventura and Ringler (2005) for details

domain-decomposition strategy for efficient implementation on distributed memory systems: each block represents a different computational processor.

4.3 Simulation

We apply this numerical method to one of the standard shallow-water test cases developed by Williamson et al. (1992) referred to as test case 5. In this test case, a flow in geostrophic balance is confronted with a large-scale orographic feature at the start of the simulation, $t = 0$. The transient forcing at $t = 0$ leads to the generation of large-amplitude gravity waves and Rossby waves. The sole forcing mechanism is the presence of the orographic forcing. While no analytical solution is known, results from high-resolution global spectral models are adequate reference solutions for the simulations conducted here (e.g., see Lipscomb and Ringler 2005).

Both simulations are stable over the course of the 15-day integration. The kinetic energy field for each simulation is shown in Fig. 17. Both simulations produce the same large-scale flow structure: an anticyclone dominates in the region of orography with a strong,

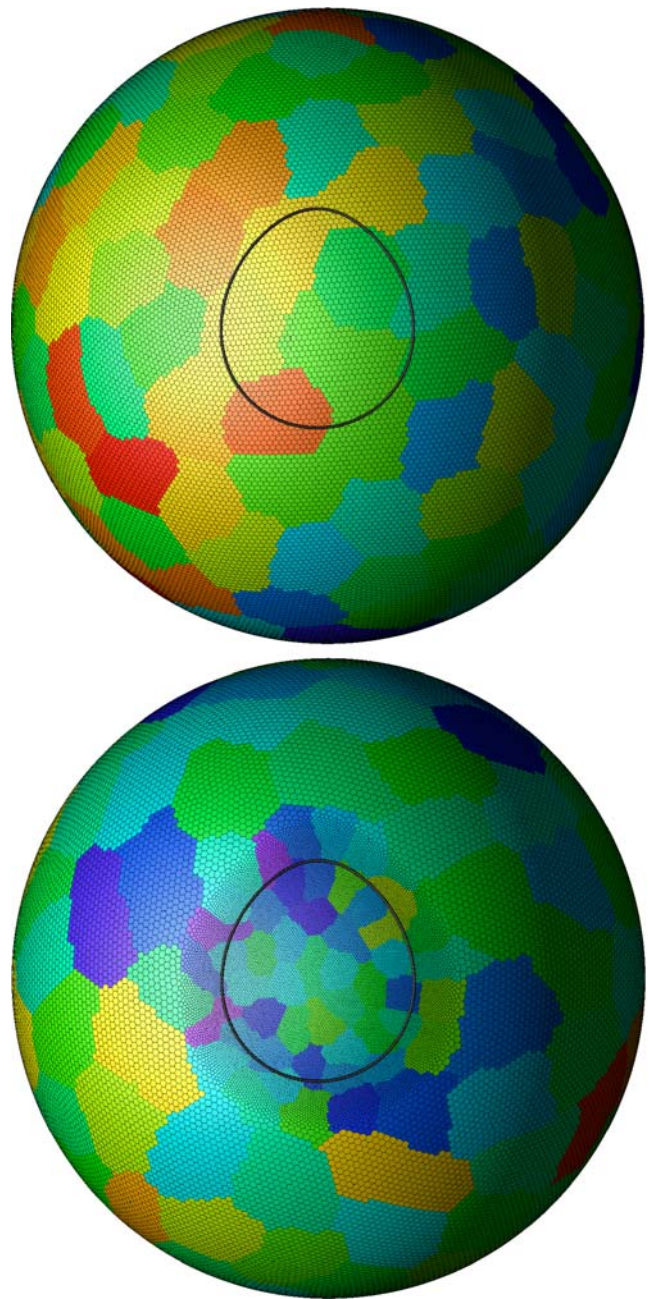


Fig. 16 Top: a SCVT using 40,962 nodes with a uniform density function. Bottom: a SCVT also using 40,962 nodes but using a nonuniform density function with high values of density occurring in the vicinity of the orography (shown by the solid black line). The variable-resolution mesh results in a minimum grid spacing of approximately 1/3 that found in the quasiuniform mesh. The colored background denotes groups of cells (blocks) that are distributed across multiple processors. The numerical method employed here defines vorticity on the SCVT nodes and mass on the dual Delaunay triangulation

stationary, low-pressure system residing immediately downstream. Both simulations produce velocities in excess of 40 m/s in the jet region.

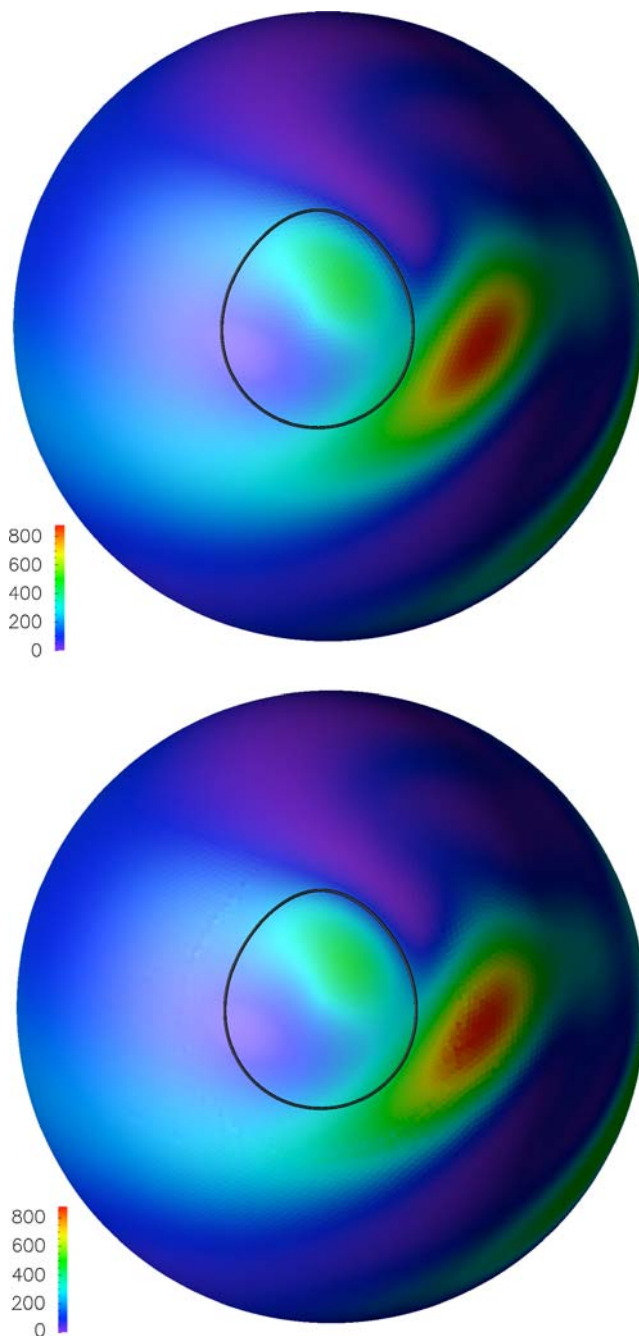


Fig. 17 Kinetic energy field at day 10 of simulation. *Top*: simulation using quasiuniform mesh. *Bottom*: simulation using variable-resolution mesh

Figure 18 shows how the error norms for each of these simulations evolve over the course of the simulation. The error is based on the deviation of the thickness field from high-resolution spectral results. The panel on the top shows the normalized L_2 -error following the procedure in Tomita et al. (2001), Eq. 17. The L_2 error norm is computed for two regions: a global domain and a local domain defined by $h_s > 0$

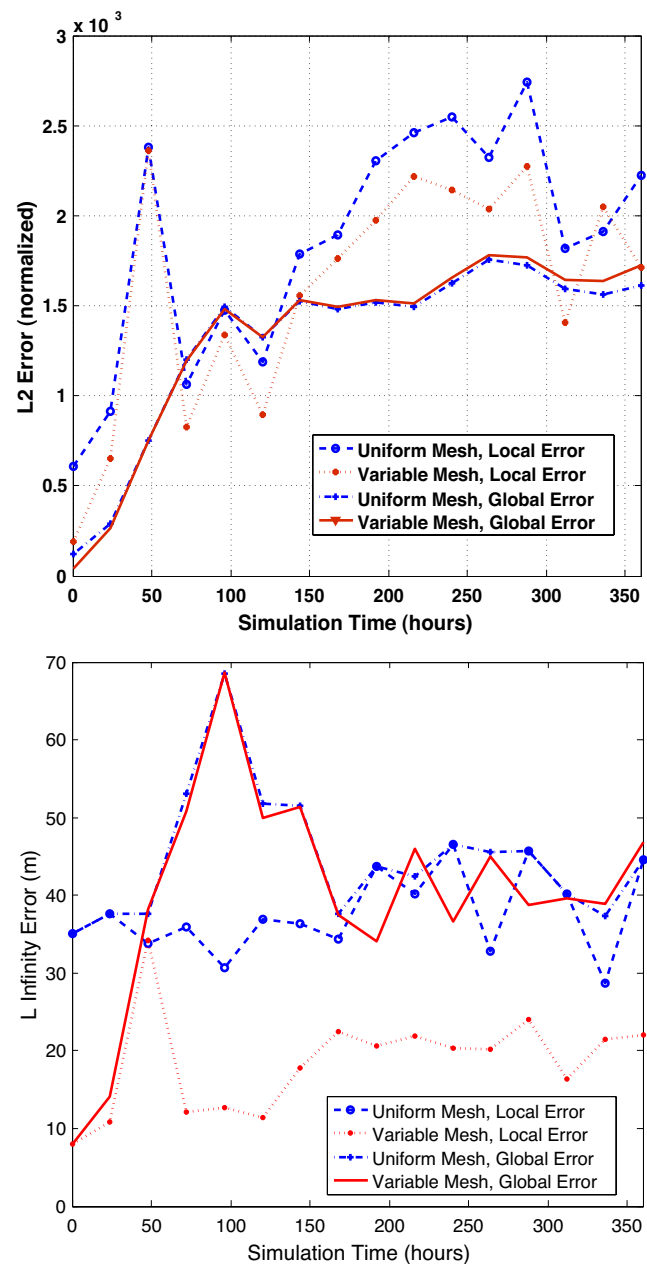


Fig. 18 *Top*: L_2 error norms for both the global domain and the local domain in the vicinity of the orography. *Bottom*: L_∞ norms for the same two domains. Each figure compares the errors produced in the uniform-mesh simulation to the errors produced in the variable-mesh simulation

that is coincident to the region of enhanced resolution. The panel on the bottom depicts the L_∞ -norm with the same layout. Since the L_2 error is normalized by the reference values, we only compare norms within the same averaging domain. When comparing the global L_2 error norms between the simulations, we find that the variable-resolution mesh provides marginal improvements only for times less than 24 h. At the early stages

of the simulation, the benefit of the variable-resolution mesh is due mostly to a better representation of the initial condition. For the remainder of the integration, the two simulations have nearly identical global L_2 error values. When we compare the local L_2 error values, we find a slightly different result; averaged over the duration of the simulation, the variable-resolution mesh reduces the error by approximately 20%. The L_∞ error values (bottom panel) exhibit a similar tendency. The variable-resolution mesh provides limited benefit in the context of global error reduction but does significantly reduce the errors in the vicinity of the orography. In this case, the variable-resolution mesh reduces the local L_∞ error norm by a factor of two as compared to the uniform mesh simulation. The implications of these findings on the merit of multiresolution CSMs will be discussed in the next section.

5 Discussion and conclusions

We have argued that the traditional paradigm of constructing IPCC-class climate models based on quasiuniform meshes will be strained in the coming decade by two mechanisms. First, each CSM component currently has one or more unresolved processes that may play an important role in the dynamics of the global climate system. These processes are either omitted altogether, exemplified by the omission of ice streams in ice sheet models, or highly parameterized, exemplified by the subgrid scale models of eddy activity in the ocean. The current and foreseeable computational resources preclude the notion of resolving these processes everywhere all of the time. Second, IPCC-class climate models will be pressed into the role of simulating regional climate change with the purpose of developing adaptation and mitigation strategies. The resolution and computational resources required for the robust simulation of regional climate change will force the climate modeling community to develop an alternative approach to complement the emerging suite of quasiuniform global CSMs.

One promising approach to meet these new challenges is based on the use of SCVTs. These tessellations (or meshes) offer many attractive qualities in the context of climate system modeling. First, since these meshes are a superset of the commonly used “icosahedral–hexagonal grids,” we can conceptually consider SCVTs to be an extension of meshes already in use today. Second, SCVTs allow for the spatial allocation of nodes in a straightforward, intuitive manner. SCVTs are generated with respect to a user-defined density function where nodes are “clustered” toward

regions of high density and away from regions of low density. Since each SCVT is associated with a Delaunay triangulation, this method is amenable to numerical methods situated on either the Voronoi diagram or the Delaunay triangulation. The proven SCVT properties related to smoothness and uniformity are conveyed to the Delaunay triangulation. If we understand a system well enough to know how to redistribute our degrees of freedom (and, hence, our computational resources), SCVTs offer an easy way to implement this redistribution. Finally, and most importantly, SCVTs are amenable to rigorous analysis from which we can make statements regarding the regularity of a given mesh and how that regularity will improve as we increase the nodes in a given domain.

We demonstrated the potential for this technique by developing example meshes for several different components of the Earth’s climate system: the Greenland ice sheet, the North Atlantic Ocean, and a generic Antarctica ice shelf–ocean interaction. Furthermore, our example numerical method developed a multiresolution mesh that is characteristic of local resolution enhancement in regional atmospheric modeling. In each of these examples, we exhibited the ability to precisely manipulate the regions of enhanced resolution through our choice of the SCVT density function. In two of the examples (Greenland and North Atlantic), the SCVT density function was developed directly from physical characteristics of the system. In the Greenland example, we used the observed ice velocity distribution to develop a SCVT density function that places increased resolution in and around ice streams. In the North Atlantic example, we constructed the SCVT density function in order to obtain meshes that are able to resolve eddy activity associated with the Gulf Stream and North Atlantic current. In each of these examples, we computed metrics that measure the quality of the mesh. In all cases, and in agreement with the theoretical underpinnings of SCVT, we found that increasing the degrees of freedom results in a uniform improvement in mesh quality. We found this consistent improvement in both the Voronoi diagrams, and in the Delaunay triangulations.

While the primary purpose of this work is to demonstrate the potential for SCVTs to produce high-quality, multiresolution meshes for climate system applications, we felt it important to also exhibit a traditional, finite-volume technique that can successfully exploit the benefits of a variable-resolution mesh. While our results in this regard are far from sufficient, we have at least produced one positive example in the context of the global shallow-water equations. Even this simple example has provided some guidance on what we should

and should not expect from multiresolution techniques, such as the one developed here. For instance, given the hyperbolic nature of many of the Earth's climate system components, it will be extremely difficult to reduce formal solution error over a wide range of conditions. Eventually, the error will become dominated by some phenomena (transient or otherwise) occurring in regions of low resolution. While this problem occurs regardless of the numerical method employed, it will likely be particularly evident when using the low-order, finite-volume methods that are ubiquitous in CSMs today. In contrast to reducing formal solution error, our emphasis will be on the formulation of robust numerical methods that produce stable, long-term simulations over a wide class of phenomena without the need for ad hoc filtering or dissipation. The driving purpose for developing multiresolution climate system components will be for the simulation of *new phenomena* requiring enhanced resolution, not necessarily for the formal reduction in solution error.

While this work has demonstrated the ability to generate high-quality meshes for a wide class of problems, the daunting challenge going forward is to develop numerical techniques that can effectively exploit these high-quality, multiresolution meshes.

Acknowledgements This work was supported by the DOE Office of Science Climate Change Prediction Program through DE-FG02-07ER64431, DE-FG02-07ER64432, and DOE 07SCPF152. The authors would like to thank Dr. Sebastien Legrand and two anonymous reviewers for their constructive comments.

References

- Adcroft A, Campin J, Hill C, Marshall J (2004) Implementation of an atmosphere-ocean general circulation model on the expanded spherical cube. *Mon Weather Rev* 132:2845–2863
- Bamber JL, Hardy RJ, Joughin I (2000) An analysis of balance velocities over the Greenland ice sheet and comparison with synthetic aperture radar interferometry. *J Glaciol* 46:67–74
- Bell RE (2008) The role of subglacial water in ice-sheet mass balance. *Nat Geosci* 1:297–304
- Bonaventura L, Ringler T (2005) Analysis of discrete shallow-water models on geodesic Delaunay grids with c-type staggering. *Mon Weather Rev* 133:2351–2373
- Collins WD, Bitz CM, Blackmon ML, Bonan GB, Bretherton CS, Carton JA, Chang P, Doney SC, Hack JJ, Henderson TB, Kiehl JT, Large WG, McKenna DS, Santer BD, Smith RD (2006) The community climate system model version 3 (CCSM3). *J Climate* 19:2122–2143
- Comblen R, Legrand S, Deleersnijder E, Legat V (2008) A finite element method for solving the shallow water equations on the sphere. *Ocean Model*. doi:10.1016/j.ocemod.2008.05.004
- Du Q, Ju L (2005) Finite volume methods on spheres and spherical centroidal Voronoi meshes. *SIAM J Numer Anal* 43:1673–1692
- Du Q, Wang D (2003) Tetrahedral mesh generation and optimization based on centroidal Voronoi tessellations. *Int J Numer Methods Eng* 56:1355–1373
- Du Q, Wang D (2005) Anisotropic centroidal Voronoi tessellations and their applications. *SIAM J Sci Comput* 26:737–761
- Du Q, Faber V, Gunzburger M (1999) Centroidal Voronoi tessellations: applications and algorithms. *SIAM Rev* 41:637–676
- Du Q, Gunzburger M, Ju L (2003a) Constrained centroidal Voronoi tessellations on general surfaces. *SIAM J Sci Comput* 24:1488–1506
- Du Q, Gunzburger M, Ju L (2003b) Voronoi-based finite volume methods, optimal Voronoi meshes and PDEs on the sphere. *Comput Methods Appl Mech Eng* 192:3933–3957
- Du Q, Wang D, Huang Z (2005) Mesh and solver coadaptation in finite element methods for anisotropic problems. *Numer Methods Partial Differ Equ* 21:859–874
- Field D (2000) Quantitative measures for initial meshes. *Int J Numer Methods Eng* 47:887–906
- Gnanadesikan A (1999) A simple predictive model for the structure of the oceanic pycnocline. *Science* 283:2077–2079
- Gersho A, Gray R (1992) Vector quantization and signal compression. Kluwer, Boston
- Giraldo F, Warburton T (2008) A high-order triangular discontinuous Galerkin oceanic shallow water model. *Int J Numer Methods Fluids* 56:899–925
- Hallberg R, Gnanadesikan A (2006) The role of eddies in determining the structure and response of the wind-driven southern hemisphere overturning: results from the modeling eddies in the southern ocean (MESO) project. *J Phys Oceanogr* 36:2232–2252
- Holland PR, Jenkins A, Holland DM (2008) The response of ice shelf basal melting to variation in ocean temperature. *J Climate* 21:2558–2572
- International Panel on Climate Change (2007) Climate change 2007: the scientific basis. International Panel on Climate Change, Valencia
- Joughin I, Gray L, Bindshadler R, Price S, Morse D, Hulbe C, Mattar K, Werner C (1999) Tributaries of West Antarctic ice streams revealed by RADARSAT interferometry. *Science* 286:283–286
- Ju L, Gunzburger M, Zhao W-D (2006) Adaptive finite element methods for elliptic PDEs based on conforming centroidal Voronoi Delaunay triangulations. *SIAM J Sci Comput* 28:2023–2053
- Lipscomb WH, Ringler TD (2005) An incremental remapping transport scheme on a spherical geodesic grid. *Mon Weather Rev* 133:2335–2350
- Lloyd S (1982) Least squares quantization in PCM. *IEEE Trans Inf Theory* 28:129–137
- MacQueen J (1967) Some methods for classification and analysis of multivariate observations. In: Proc. fifth Berkeley symposium on mathematical statistics and probability, vol I. University of California, Berkeley, pp 281–297
- McGregor JL (1996) Semi-Lagrangian advection on a conformal cubic grid. *Mon Weather Rev* 124:1311–1322
- Maltrud ME, McClean JL (2004) An eddy-resolving global 1/10 degree ocean simulation. *Ocean Model* 8:31–54
- Nair R, Thomas S, Loft R (2005) A discontinuous Galerkin global shallow water model. *Mon Weather Rev* 133:867–888
- Newman BD, Wilcox BP, Archer S, Breshears DD, Dahm CN, Duffy CJ, McDowell NG, Phillips FM, Scanlon BR, Vivoni ER (2006) The ecohydrology of arid and semiarid environments: a scientific vision. *Water Resour Res* 42:W06302. doi:10.1029/2005WR004141

- Okabe A, Boots B, Sugihara K, Chiu S (2000) Spatial tessellations: concepts and applications of Voronoi diagrams, 2nd edn. Wiley, Chichester
- Randall DA, Ringler TD, Heikes RP, Jones P, Baumgardner J (2002) Climate modeling with spherical geodesic grids. *Comput Sci Eng* 4:32–41
- Renka R (1999) ALGORITHM 772. STRIPACK: Delaunay triangulation and Voronoi diagrams on the surface of a sphere. *ACM Trans Math Softw* 23:416–434
- Rignot E, Bamber JL, van den Broeke MR, Davis C, Li Y, van de Berg WJ, van Meijgaard E (2008) Recent Antarctic ice mass loss from radar interferometry and regional climate modelling. *Nat Geosci* 1:106–110
- Rignot E, Casassa G, Gogineni P, Krabill W, Rivera A, Thomas R (2004) Accelerated ice discharge from the Antarctic Peninsula following the collapse of Larsen B ice shelf. *Geophys Res Lett* 31(18):L18401. doi:[10.1029/2004GL020697](https://doi.org/10.1029/2004GL020697)
- Ringler TD, Heikes RP, Randall DA (2000) Modeling the atmospheric general circulation using a spherical geodesic grid: a new class of dynamical cores. *Mon Weather Rev* 128:2471–2490
- Satoh M, Matsuno T, Tomita H, Miura H, Nasuno T, Iga S (2008) Nonhydrostatic icosahedral atmospheric model (NICAM) for global cloud resolving simulations. *J Comput Phys* 227:3486–3514
- Schoof C (2007) Ice sheet grounding line dynamics: steady states, stability, and hysteresis. *J Geophys Res* 112(F3):F03S28
- Smith RD, Maltrud ME, Bryan FO, Hecht MW (2000) Numerical simulation of the north atlantic ocean at 1/10. *J Phys Oceanogr* 30:1532–1561
- St-Cyr A, Jablonowski C, Dennis JM, Tufo HM, Thomas SJ (2007) A comparison of two shallow water models with non-conforming adaptive grids. *Mon Weather Rev* 136:1898–1922
- Stuhne G, Peltier W (2006) A robust unstructured grid discretization for 3-dimensional hydrostatic flows in spherical geometry: a new numerical structure for ocean general circulation modeling. *J Comput Phys* 213:704–729
- Tomita H, Tsugawa M, Satoh M, Goto K (2001) Shallow water model on a modified icosahedral geodesic grid by using spring dynamics. *J Comput Phys* 174:579–613
- Tomita H, Miura H, Iga S, Nasuno T, Satoh M (2007) A global cloud-resolving simulation: preliminary results from an aqua planet experiment. *Geophys Res Lett* 32:L08805. doi:[10.1029/2005GL022459](https://doi.org/10.1029/2005GL022459)
- Williamson DL, Drake JB, Hack J, Jacob R, Swartztrauber PN (1992) A standard test for numerical approximation to the shallow water equations in spherical geometry. *J Comput Phys* 102:211–224